# Bayesian calibration of a natural state geothermal reservoir model, Krafla, north Iceland

Samuel Scott[1], John P O'Sullivan[2], Oliver J Maclaren[3], Ruanui Nicholson[3], Cari Covell[4], Juliet Newson[4], and María S Gujónsdóttír[4]

[1]University of Iceland
[2]University of Auckland
[3]The University of Auckland
[4]Reykjavik University

November 24, 2022

**Abstract**

The Krafla area in north Iceland hosts a high-temperature geothermal system within a volcanic caldera. Temperature measurements from boreholes drilled for power generation reveal enigmatic contrasts throughout the drilled area. While wells in the western part of the production field indicate a 0.5-1 km thick near-isothermal (~210 °C) liquid-dominated reservoir underlain by a deeper boiling reservoir, wells in the east indicate boiling conditions extending from the surface to the maximum depth of drilled wells (~2 km). Understanding these systematic temperature contrasts in terms of the subsurface permeability structure and overall dynamics of fluid flow has remained challenging. Here, we present a new numerical model of the natural, pre-exploitation state of the Krafla system, incorporating a new geologic/conceptual model and a version of TOUGH2 extending to supercritical conditions. The model shows how the characteristic temperature distribution results from structural partitioning of the system by a rift-parallel eruptive fissure and an aquitard at the transition between deeper basement intrusions and high-permeability extrusive volcanic rocks. As model calibration is performed using a Bayesian framework, the posterior results reveal significant uncertainty in the inferred permeability values for the different rock types, often exceeding two orders of magnitude. While the model shows how zones of single-phase vapor develop above the deep intrusive heat source, more data from deep wells is needed to better constrain the extent and temperature of the deep vapor zones. However, the model suggests the presence of a significant untapped resource at Krafla.

# Bayesian calibration of a natural state geothermal reservoir model, Krafla, north Iceland

**S. W. Scott[1,2], J. P. O'Sullivan[3], O. J. Maclaren[3], R. Nicholson[3], C. Covell[1], J. Newson[1], M. S. Guðjónsdóttir[1]**

[1]Department of Engineering, Reykjavik University, Reykjavik, Iceland
[2]Institute of Earth Sciences, University of Iceland, Reykjavik, Iceland
[3]Department of Engineering Science, The University of Auckland, Auckland, New Zealand

**Key Points:**

- We perform MCMC calibration of a 3-D natural state reservoir model of the Krafla geothermal system
- Posterior results indicate that the uncertainty of inferred permeability values is underestimated using deterministic approaches
- One of the first reservoir models of an exploited geothermal system extending to the deep, supercritical roots near the heat source

Corresponding author: Samuel Scott, `samuelwarrenscott@gmail.com`

## Abstract

The Krafla area in north Iceland hosts a high-temperature geothermal system within a volcanic caldera. Temperature measurements from boreholes drilled for power generation reveal enigmatic contrasts throughout the drilled area. While wells in the western part of the production field indicate a 0.5-1 km thick near-isothermal (∼210 °C) liquid-dominated reservoir underlain by a deeper boiling reservoir, wells in the east indicate boiling conditions extending from the surface to the maximum depth of drilled wells (∼2 km). Understanding these systematic temperature contrasts in terms of the subsurface permeability structure has remained challenging. Here, we present a new numerical model of the natural, pre-exploitation state of the Krafla system, incorporating a new geologic/conceptual model and a version of TOUGH2 extending to supercritical conditions. The model shows how the characteristic temperature distribution results from structural partitioning of the system by a rift-parallel eruptive fissure and an aquitard at the transition between deeper basement intrusions and high-permeability extrusive volcanic rocks. As model calibration is performed using a Bayesian framework, the posterior results reveal significant uncertainty in the inferred permeability values for the different rock types, often exceeding two orders of magnitude. While the model shows how zones of single-phase supercritical vapor develop above the deep intrusive heat source, more data from deep wells is needed to better constrain the extent and temperature of the deep supercritical zones. However, the model suggests the presence of a significant untapped resource at Krafla.


## 1 Introduction

Geothermal systems develop in response to elevated heat fluxes in areas of active magmatism and volcanism (Stimac et al., 2015; Jolie et al., 2021). Hydrothermal convection in permeable rocks results in cooling of subsurface intrusions and the development of boiling zones (Hayba & Ingebritsen, 1997; Scott et al., 2016). Natural state geothermal reservoir models describe the subsurface temperature/pressure distribution, the location and depth of boiling zones, and the rates of heat and mass transport prior to the onset of exploitation (M. O'Sullivan et al., 2001; M. O'Sullivan & O'Sullivan, 2016). The sustainable level of power generation that a geothermal system can support is intimately linked to the subsurface dynamics of fluid flow and heat transfer, which are elucidated by the natural state model (Gunnarsson et al., 2010; M. O'Sullivan & O'Sullivan, 2016). Even in geothermal systems such as Krafla that have been exploited for several decades, there is a paucity of data needed to constrain the system structure, and the uncertainty of natural state models is significant. As consideration of this uncertainty can help generate more realistic predictions of the impact of production on the system behavior, it is thus essential to ensuring that reservoir models effectively contribute to sustainable management of geothermal resources.

The foundation of the natural state model is the conceptual model describing the structure of a geothermal system based on an integration of available geologic, geophysical, hydrologic and geochemical data (Cumming, 2016a). The calibration of natural state geothermal reservoir models involves finding geologically-reasonable model parameters consistent with the conceptual model as well as field observations prior to exploitation, including measured temperatures/pressures, the locations of discharge zones, and rates of surface heat transport. Modern software tools such as Leapfrog Geothermal facilitate the development of a three-dimensional geologic model based on surface mapping and downhole data, and the design and export of numerical grids populated with rock types according to the geologic model (Newson et al., 2012; Milicich et al., 2018; Popineau et al., 2018). This ensures a close coupling between the conceptual/geologic model and the reservoir model.

One of the key parameters requiring calibration in natural state geothermal reservoir models is the anisotropic permeability of the different rock types and their spatial distribution. The other key parameter involved in natural state model calibration consists of the heat and mass sources applied at the base of the computational model, which control the strength and location of fluid upflow zones. The inherent uncertainty of these parameters makes calibration of natural state geothermal reservoir models challenging (M. O'Sullivan & O'Sullivan, 2016). While manual adjustment of input parameters remains the dominant approach to model calibration (M. O'Sullivan & O'Sullivan, 2016), a variety of inverse modeling tools are available to automate the calibration process, including iTOUGH2 (Finsterle, 2007) and PEST (Doherty, 2015). These methods use gradient-based methods to find the minimum of a sum-of-squares type objective function based on matching the measured and simulated temperatures. Uncertainty metrics for model parameters can be constructed from the derivatives of the local cost function (Aster et al., 2018). However, the objective function may have many local minima (Plasencia et al., 2014), and the global minimum may reside in a part of the parameter space that is inconsistent with field and/or laboratory measurements.

The Bayesian approach to inverse modeling naturally allows for specification of prior uncertainty of input parameters and quantification of uncertainty in the estimated parameters (Mosegaard & Sambridge, 2002; Tarantola, 2005; Kaipio & Somersalo, 2006; Gelman et al., 2013). In the Bayesian framework, the solution to the inverse problem is a posterior probability density over the model parameters, the statistics of which are usually obtained using Markov chain Monte Carlo (MCMC) sampling methods (Andrieu et al., 2003). One major drawback of the MCMC approach for inverse modeling of geothermal systems is the intensive computational cost required to repeatedly evaluate the forward model describing multi-phase fluid flow in a porous medium. This is particularly true for natural state models, which are run to long times (ca. $10^6$ years) in order to achieve a steady-state configuration. Presently, MCMC sampling for geothermal reservoir model calibration is only feasible through the use of a coarsened, less computationally-expensive model for MCMC sampling instead of a finer, more computationally-expensive models (Cui et al., 2011; Cui, Fox, & O'Sullivan, 2019; Cui, Fox, Nicholls, & O'Sullivan, 2019; Maclaren et al., 2020). Different strategies have been developed to deal with the additional error introduced by using the coarsened model in place of the finer model. Cui et al. (2011) developed a sophisticated delayed acceptance algorithm that adaptively builds a stochastic model of this error. Maclaren et al. (2020) present an alternative approach that incorporates the posterior-informed approximation errors into a hierarchical framework. One advantage of the latter approach is its relative simplicity, as only a relatively small number of realizations of the fine model are required to enable sampling from the target posterior. Furthermore, the approach of Maclaren et al. (2020) is essentially independent of the specific MCMC sampling algorithm used.

In this study, we present a new natural state reservoir model of the Krafla geothermal system in northeast Iceland. Although the Krafla system has been under exploitation for more than 4 decades, the last published natural state reservoir model of the area dates back to the 1980s and was a 2-dimensional model (Bödvarsson et al., 1984). Since that time, the drilling of additional boreholes has provided significantly more geologic and hydrologic data, and computational abilities have increased tremendously. For example, recent enhancements to TOUGH2 extend the applicability of the numerical simulation software to the deep, supercritical (>375 ℃) roots (Magnusdóttir & Finsterle, 2015; J. O'Sullivan et al., 2015; M. O'Sullivan & O'Sullivan, 2016; J. O'Sullivan et al., 2020). Such conditions are present at depth in Krafla, as evidenced by the drilling of the Iceland Deep Drilling Project (IDDP) well IDDP-1, which encountered a shallow magmatic intrusion at ∼2 km depth and discharged a 440 ℃ single-phase vapor (Ármannsson et al., 2014). We adapt the Bayesian hierarchical approach of Maclaren et al. (2020) to perform the model calibration and quantify the uncertainty in the inferred permeability structure. This study highlights the potential for Bayesian approaches to enable better consideration of geologic uncertainty during natural state model calibration.

# 2 The Krafla Geothermal System

## 2.1 Geologic background

The Krafla area hosts a central volcano approximately 20 km in diameter sitting astride a 90 km long NNE-SSW trending fissure swarm (Sæmundsson, 1991; Hjartardóttir et al., 2012) (Figure 1). Krafla is one of five active volcanic centers arranged in en-echelon fashion within the northern volcanic zone (NVZ) in northeast Iceland along with Kverkfjöll, Askja, Fremrinámur and Theistareykir (P. Einarsson, 2008; Hjartardóttir et al., 2016). The central volcano has developed an 8-10 km diameter caldera structure that formed around 110 ky ago (Sæmundsson, 1991). Volcanism in the caldera dominantly occurs as basaltic fissure eruptions and dike injections, along with intermittent eruptions of more silicic magmas (Jónasson, 1994). About 20 eruptions have taken place within the Krafla caldera during the postglacial era (Sæmundsson, 1991), most recently in 1975-1984 C.E. (A. Björnsson et al., 1977; P. Einarsson, 1991). During this eruption sequence (often referred to as the 'Krafla fires'), seismic studies delineated volumes between 3-7 km depth in the subsurface with S-wave shadows, which were interpreted to represent a network of basaltic sills and intrusions underlying the central part of the caldera (P. Einarsson, 1978). More recently, rhyolitic magma bodies were encountered around 2 km depth during the drilling of the wells KJ-39 and IDDP-1 (Mortensen et al., 2010; Elders et al., 2011). Petrologic data suggest a link between the IDDP-1 rhyolite and the rhyolite erupted in 1724 C.E. during the formation of Víti, a small (∼300-m-diameter) maar located 0.5 km to northeast of IDDP-1, suggesting the subsurface rhyolite may extend throughout the center of the caldera (Rooyakkers et al., 2021).

The geologic structure of the Krafla area has been intensively studied (Stefánsson, 1981; Sæmundsson, 1991; Ármannsson et al., 1987; Sæmundsson, 2008; Mortensen et al., 2009; Weisenberger et al., 2015). Above 0.4-1 km b.s.l., the subsurface lithology in the central part of the caldera mainly consists of extrusive igneous rocks, including sub- or intraglacially-erupted basaltic hyaloclastite (Jakobsson & Guðmundsson, 2008) and subaerially erupted basaltic lava flows. Doleritic and gabbroic intrusions dominate at greater depths, along with minor granophyre and other silicic intrusions (Mortensen et al., 2015). The depth to the intrusive basement varies from about 0.8-1.1 km in the central part of the caldera to about 1.5-1.6 km in the southern part (Weisenberger et al., 2015). The rocks at Krafla undergo alteration as a result of high-temperature fluid-rock interaction, with the alteration mineralogy following the typical depth- and temperature-dependent zonation characteristic of Icelandic geothermal systems (Kristmannsdóttir, 1979; Á. Sveinbjörnsdóttir, 1992). With increasing depth and temperature, these alteration zones are the smectite-zeolite zone, the mixed-layer clay zone, the chlorite-epidote zone, the epidote zone, and the epidote-actinolite zone. The intensity of alteration is very variable but often increases with depth (Mortensen et al., 2014). Alteration and compaction reduces the high primary porosity and permeability of the extrusive volcanic rocks (Weisenberger & Selbekk, 2009; Thien et al., 2015; Heap et al., 2020; Eggertsson, Lavallée, et al., 2020).

A total of 43 deep geothermal wells have been drilled in the central part of the Krafla caldera to provide steam to a geothermal power plant that currently generates 60 MWe (Figure 2). A smaller geothermal power plant currently generating 3 MWe is located in Bjarnarflag (Fig. 1), approximately 11 km to the south of Krafla. Bjarnarflag is located close to Námafjall, an area with abundant fumarole degassing (Oskarsson, 1984), and was the site of an explosive eruption of a basaltic tephra through a geothermal borehole during the Krafla fires (Larsen et al., 1979). While the Krafla and Bjarnarflag systems may be hydraulically connected via the high permeability NNW-SSE trending fissure swarm, a separate dyke complex is believed to be the heat source for Námafjall (Gylfadóttir, 2013; Drouin et al., 2017).

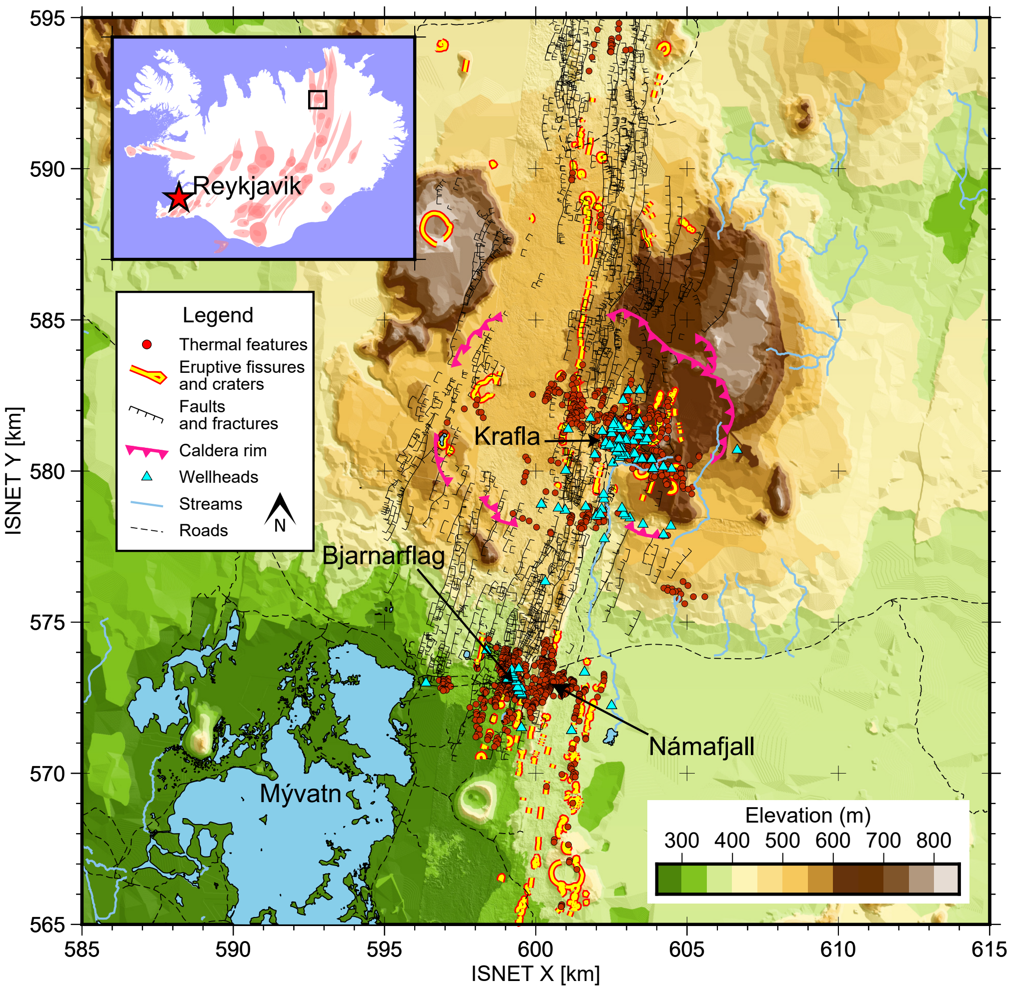


**Figure 1.** Topographic map of the Krafla area, showing the locations of drilled wells (blue triangles), thermal features (red circles), eruptive fissures (yellow/red lines), faults and fractures (hatchured black lines), the caldera rim (pink toothed line), streams and water bodies (light blue), and roads (dashed black lines). The inset shows the location of the Krafla area in north-east Iceland and the locations of other volcanic areas and fissure swarms. Coordinates are shown in ISNET16 (same as Lambert 95).

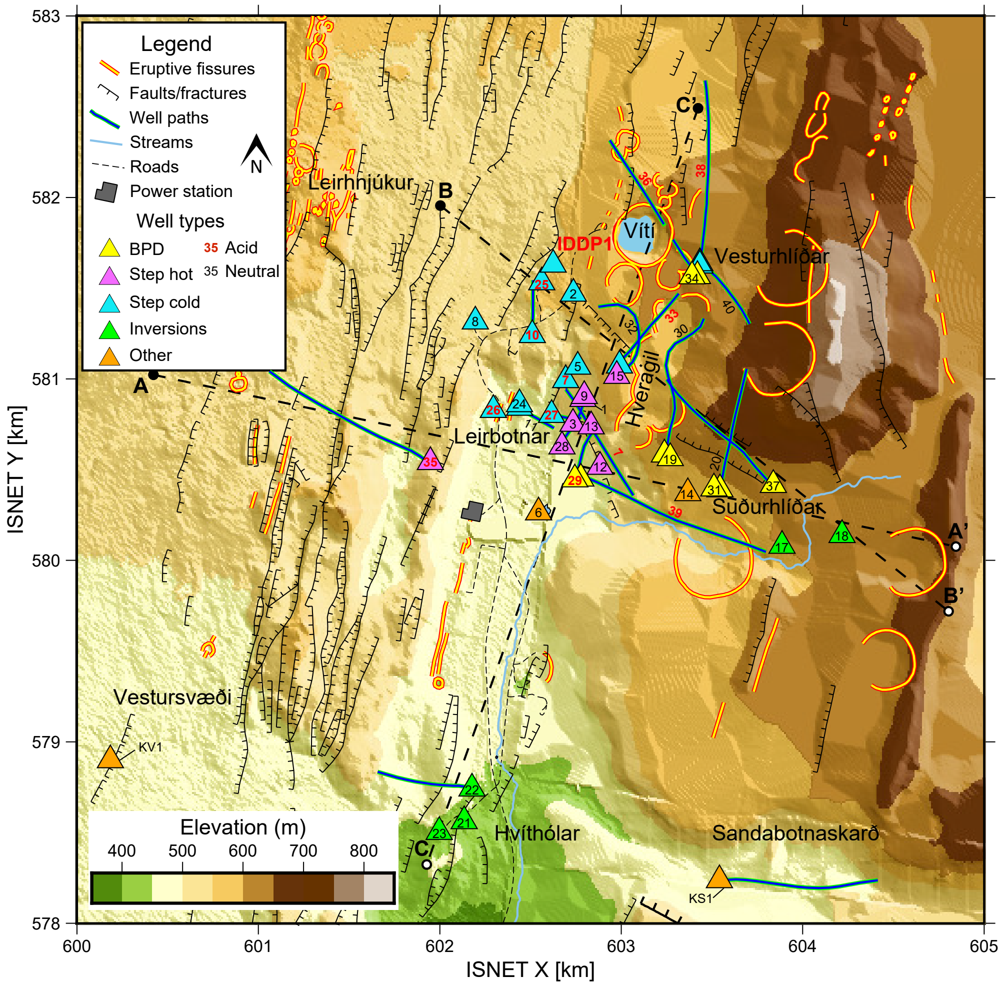


**Figure 2.** Topographic map of the main production area in the center of the Krafla caldera. Locations of wellheads used to calibrate the numerical model in this study are shown as colored triangles. The wells are grouped according to the the characteristic measured temperature profiles: 1) Yellow triangles indicate wells with temperatures following the boiling point with depth (BPD) to ≥1.5-2 km depth. 2) Purple triangles indicate wells that feature an isothermal zone with temperatures 210-225 °C (Step hot). 3) Light blue triangles indicate wells with an isothermal zone at temperatures ≤210 °C (Step cold). 4) Green triangles indicate wells that show temperature inversions, i.e. decreasing temperatures with increasing depth below a certain depth. 5) Orange triangles indicate wells with other characteristics. The traces of directional wells are shown as dark blue lines. The surface traces of the cross-sections shown in Figure 4 are shown with dashed black lines. The numbers indicate the well numbers, with red numbers corresponding to acid wells (see text).

## 2.2 Conceptual model of the Krafla geothermal system

Several conceptual models of the geothermal resource in the Krafla area have been published (Stefánsson, 1981; Ármannsson et al., 1989; Mortensen et al., 2015; Weisenberger et al., 2015; Árnason, 2020). The conceptual model below synthesizes insights from these previous studies and others. On the basis of differing production characteristics and temperature-depth relations, the drilled area at Krafla can be divided into five subfields: (1) Leirbotnar, located to the west of the Hveragil eruptive fissure, (2) Suðurhlíðar, located to the east of Hveragil, (3) Hvíthólar, located on the southern rim of the caldera, (4) Vestursvæði, located to the north of Suðurhlíðar and (5) Sandabotnaskarð, located to the south of Suðurhlíðar. The natural state temperatures from 40 deep geothermal wells grouped by subfield are shown in Figure 3.

Downhole temperature measurements in Leirbotnar reveal two distinct reservoirs: an upper sub-boiling reservoir extending from -0.5 to -1 km a.s.l. with a remarkably constant temperature between 190-220 °C, and a deeper boiling reservoir that reaches temperatures up to 350 °C (Fig. 3a). In this study, we distinguish between wells in the Leirbotnar subfield with temperatures 210-225 °C (Step hot in Fig. 2) or $\leq$210 °C (Step cold) within the isothermal zone. Wells with a hotter isothermal zone tend to cluster around the southwest of the Hveragil eruptive fissure, while the wells with the cold isothermal zone are spread further to the northwest, suggesting a gradient with increased mixing of cooler recharging fluids to the northwest. The steep, near-linear temperature gradient at the base of the isothermal zone suggests the presence of a low permeability aquitard separating the upper liquid reservoir from the deeper boiling reservoir (Stefánsson, 1981; Bödvarsson et al., 1984). Comparison of the temperature measurements with the geologic data (Mortensen et al., 2015; Weisenberger et al., 2015) suggests that the transition between the upper sub-boiling reservoir and the deeper boiling reservoir coincides with a transition between shallower extrusive volcanics and deeper crystalline basement intrusions.

In contrast to the characteristic step-increase seen in Leirbotnar, wells in the Suðurhlíðar subfield show downhole temperatures indicating boiling conditions from the surface to depths of at least -1.5 km a.s.l. (Fig. 3b). The lack of the step increase in temperature for the wells in Suðurhlíðar suggests that the inferred aquitard underlying Leirbotnar does not extend across the Hveragil eruptive fissure (Stefánsson, 1981; Bödvarsson et al., 1984), or that higher subsurface fluid pressures in areas beneath Krafla mountain prevents cold recharge from the north (Arnórsson, 1995). The Suðurhlíðar subfield is believed to be bounded to the east by a sub-vertical, rift-parallel fracture system (Stefánsson, 1981; Bödvarsson et al., 1984) and to the south by a WNW-ESE oriented transform structure, which has been inferred along the on the basis of structural, gravity and resistivity data (Árnason, 2020; Liotta et al., 2021). The intersection of such transform structures with the rift is believed to enhance permeability and localize fluid upflow at depth (Khodayar et al., 2018; Liotta et al., 2021). The Vesturhlíðar subfield is located to the north of Suðurhlídar and to the east of the Víti maar, and shows wells that follow the BPD over the entire depth range with the characteristic "step" increase.

Several wells throughout Krafla have encountered high acidity fluids in the deeper boiling reservoir (K. Einarsson et al., 2010; Ármannsson et al., 2015) that are believed to originate from condensation of liquid from HCl-bearing vapor during ascent, depressurization, and mixing with cooler fluids (Heřmanská et al., 2019). The relatively wide geographic distribution of acid wells (labeled with red text in Figs. 2 and 4) suggests that HCl-bearing superheated/supercritical vapor is present at depths $>$ 2 km b.s.l. over a wide area in the center of the Krafla caldera (K. Einarsson et al., 2010; Ármannsson et al., 2015).

Wells drilled in the Hvítholar area show temperature inversions, with a boiling reservoir reaching 250–260 °C extending to approximately -0.5 km a.sl. underlain by sharply decreasing temperatures to 170–190 °C. Such temperature inversions are often associa-

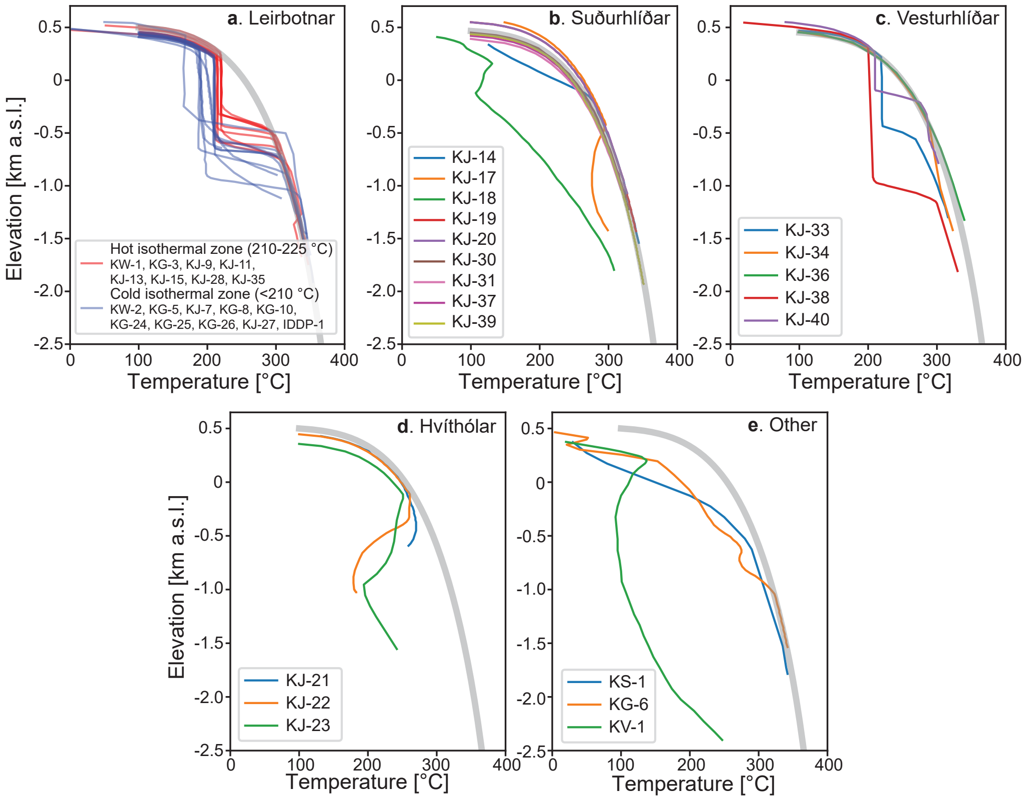


**Figure 3.** Natural state temperature-depth profiles for wells used to calibrate the numerical model. Wells are grouped by subfield and the overall style of temperature-depth profile: a) Leirbotnar, grouped on whether the temperature in the isothermal zone is 210-225 ℃ (Step hot in Fig. 3) or ≤210 ℃ (Step cold in Fig. 3), b) Suðurhlíðar c) Vesturhlíðar, d) Hvíthólar, and e) Other, including wells from Vestursvæði, Sandabotnaskarð, and KJ-06, the southernmost well in Leirbotnar. The boiling point with depth curve is shown in light gray, assuming a water table depth of 0.5 km a.s.l.

ted with lateral outflow of hot fluid below the clay cap, accompanied by recharge of cooler waters at greater depths (Grant et al., 2011). However, Arnórsson (1995) suggested that the temperature reversals represent ascending fluid along the rims of the caldera, and Árnason (2020) argued that the temperature inversions represent the waning stages of a geothermal system after the deep heat source has been extinguished by hydrothermal convection. Well KS-1 (Fig. 3e) drilled in the Sandabotnaskarð area, east of Hvítholar, shows temperatures following the BPD between -0.5 and -1.5 km a.s.l. but lower temperatures at shallower depths. These high temperatures suggest the potential that the high-temperature system may extend to the south of Suðurhlíðar. In contrast, well KV-1 in Vestursvæði, to the west of Hvíthólar, shows temperatures up to 150 °C above 0 km a.s.l. and lower temperatures at greater depths, suggesting shallow outflow of hot fluid and circulation of cooler surface-derived waters at depth.

The conceptual model for the Krafla system is summarized in Figure 4. The magmatic heat source is a complex of basaltic sills and dykes located at $\geq$2.5-3 km b.s.l., corresponding to the attenuating body identified during the volcano-tectonic episode between 1977-1984 (P. Einarsson, 1978). The rhyolitic magma encountered during drilling of IDDP-1 in the northern part of Leirbotnar and KJ-39 along the southern rim of Suðurhlíðar corresponds to local magma pockets with thickness $\leq$0.2 km, an interpretation consistent with evidence from seismic (Kim et al., 2017, 2018; Schuler et al., 2016) and resistivity (Lee et al., 2020) studies. At depths $\geq$2 km b.s.l., this fluid ascending above the heat source is a single-phase vapor, which depressurizes, cools, and condenses to form an acidic liquid condensate (Heřmanská et al., 2019), representing the deep reservoir fluids produced by the 'acid' wells (labeled in red in Fig. 4). The main location of fluid upflow is along and west of the Hveragil eruptive fissure, which features the high vertical and rift-parallel permeability but relatively low cross-rift permeability. A low permeability aquitard situated at the transition between the underlying basement intrusions and shallower volcanics that effectively separates the upper sub-boiling reservoir from the deeper boiling reservoir in Leirbotnar (Stefánsson, 1981; Bödvarsson et al., 1984). To the west of the Hveragil, this aquitard is not present or not as tight, allowing the formation of a vertically-extensive boiling zone in the Sudurhlíðar area. Variable mixing of fluid ascending along Hveragil with cold water from the north (blue + sign in Fig. 4a) controls the spatial distribution of temperature in the upper sub-boiling aquifer. We interpret the temperature inversions measured in the Hvíthólar area as the result of southward outflow of hot water originating from the main production field along the axis of the rift. The deuterium and oxygen-18 composition of the geothermal fluid at Krafla (A. E. Sveinbjörnsdóttir et al., 1986; Darling & Ármannsson, 1989; Pope et al., 2015) indicate that the main recharge area for the geothermal system comes from the highlands to the north of the main production field. However, further deep recharge from the south and west, as suggested by the relatively cold temperatures measured in Vestursvæði indicating cold cross-flow.

## 3 Methodology

The model developed in this study incorporates several components:

1. Fine-scale and coarse-scale reservoir models based on the conceptual model of the system (Figure 5)
2. A numerical method that accurately models flow of multi-phase, variably miscible fluids, with a range of applicability extending to >375 °C
3. A hierarchical Bayesian approach incorporating a posterior-informed approximation error model

Here, we briefly describe the numerical method and hierarchical Bayesian approach, which have been published previously (Pruess et al., 2012; Maclaren et al., 2020), and focus on description of the model setup.

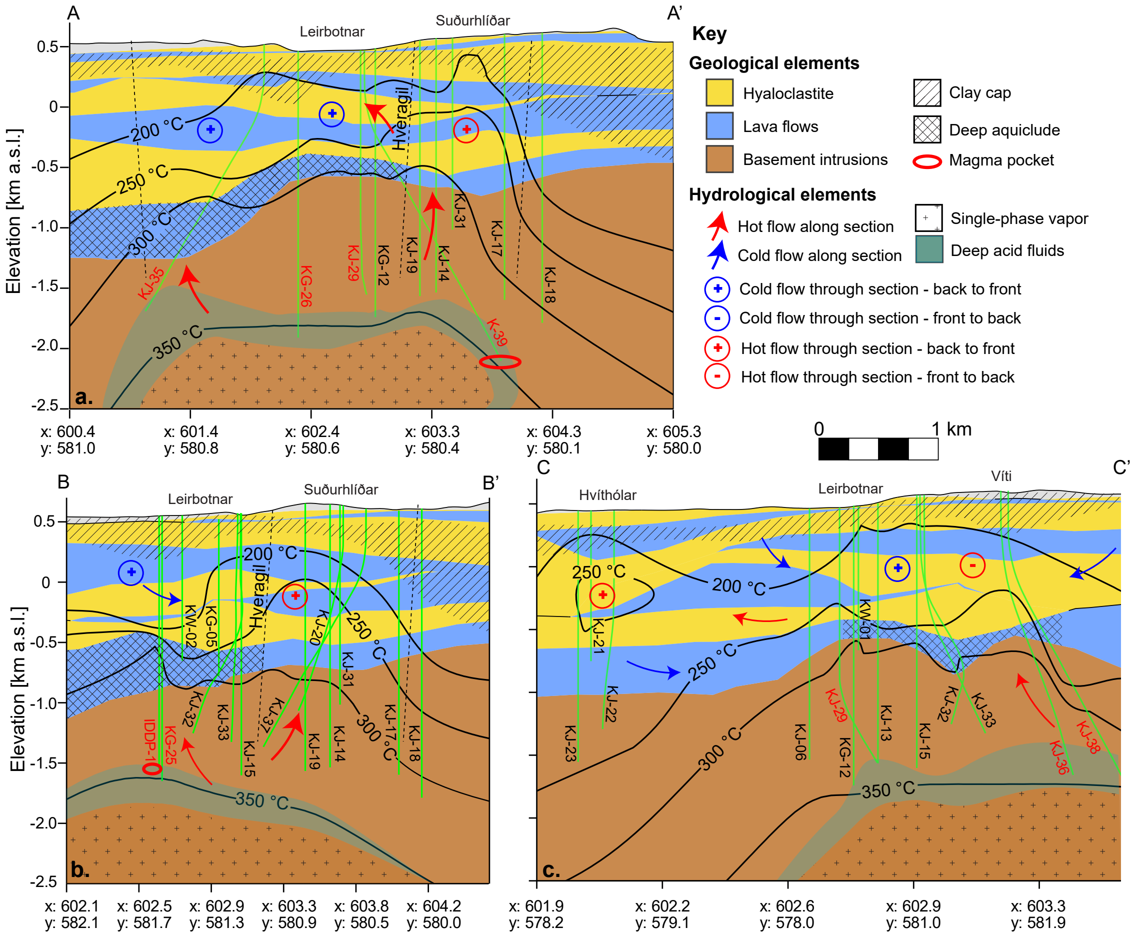


**Figure 4.** Geologic-conceptual model of the Krafla system. The geologic and alteration model is based on Weisenberger et al. (2015). The surface traces of the cross sections are shown in Figure 2. **a**. An ESE-WNW cross-section across Leirbotnar and Suðurhlíðar. **b**. A NW-SW cross-section across the northern part of Leirbotnar and Suðurhlíðar. **c**. A N-S cross-section across the Víti caldera to Hvíthólar. The lithologic model describes a succession of hyaloclastite (yellow) and lava flows (blue) underlain by basement intrusions (brown). The cap rock (hatching) is based on the mapped distribution of smectite-zeolite and mixed-layer clay alteration facies. The deep aquitard (cross-hatching) is inferred to correlate with the basal lava flow west of Hveragil. Cross sections also show well traces (green lines), temperature isotherms derived from natural state temperature measurements (solid black lines), as well as select structural features (dashed black lines). Red/blue arrows indicate the schematic direction of flow of hot or cold water, respectively. Plus/minus sign enclosed in a circle indicates flow of hot or cold into or out of the section, respectively. Zones of single-phase vapor and deep acid fluids (see text) are shown with crosses and dark blue color, respectively.

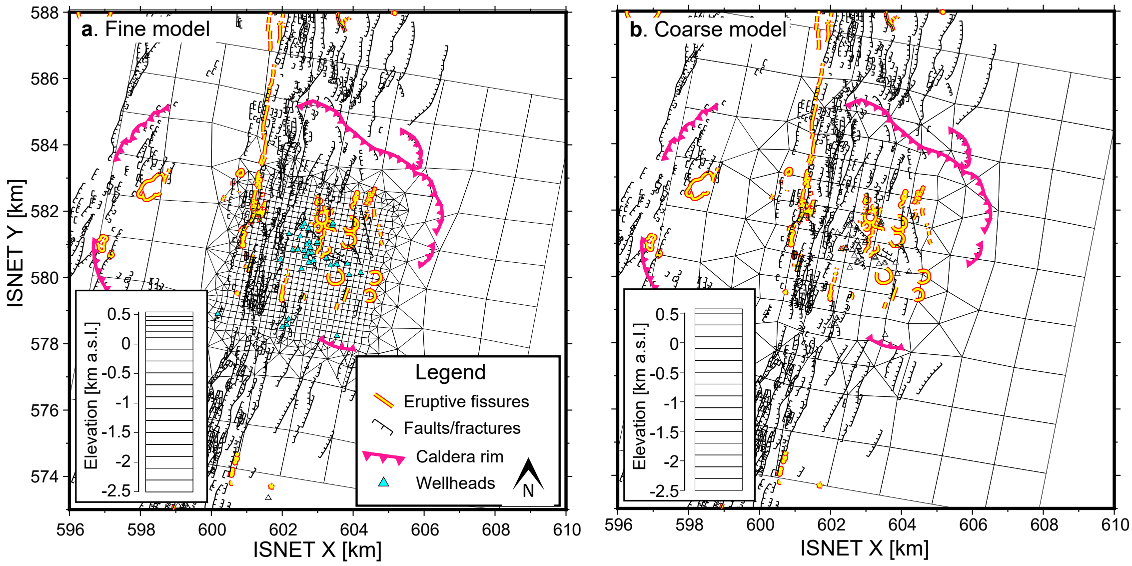


**Figure 5.** Grid structure of the a) fine-scale and b) coarse-scale models used in this study.

### 3.1 Model Structure

Figure 5 shows the discretization and layer structure of the fine and coarse scale models developed in this study. The numerical grid extends ∼14 km in the N-S direction, ∼12.5 km in the E-W direction, and from the surface to -2.5 km a.s.l. The grid is rotated 11° along the main axis of rifting. The coarse- and fine-scale models consist of 2551 and 17193 grid blocks in 17 and 22 layers, respectively, with increasing resolution towards the surface. The maximum horizontal resolution of the grid blocks in the fine- and coarse-scale model is 0.15 km$^2$ and 0.5 km$^2$, respectively.

The numerical grid was first designed in Leapfrog Geothermal ®, refined using PyTOUGH (Croucher, 2011; J. O'Sullivan et al., 2015), and then imported back into Leapfrog Geothermal in order to populate rock types in the model based on the geologic model (Mortensen et al., 2015; Weisenberger et al., 2015; Scott et al., 2019). The numerical model considers 14 different rock types (Table 1). The extrusive volcanic rocks in the upper 1-1.5 km of the system consist of 4 lava flow units (LV001-LV004) and 3 hyaloclastite units (HY001-HY003). Two different basement intrusion rock types were defined for the geothermal system in the center of the caldera: BASE1, which comprises the majority of the basement, and BASE2, which was defined locally at the base of wells IDDP-1 and KJ-39 where magmatic intrusions were encountered. Two different fault rock types were defined: 1) TVFLT with relatively high cross-rift permeability, and low rift-parallel permeability, and 2) BARFT with relatively high rift-parallel permeability and low cross-rift permeability. A clay cap rock type (CLAYC) with relatively low permeability was defined and the geometry of the clay cap was constrained based on the alteration model and resistivity data. Two rock types were defined for the area outside of the main area of the geologic model: 1) OUTBS, defining the outer basement below 1 km b.s.l., and 2) OUTER, defining the upper volcanic sequence above 1 km b.s.l. As described in the conceptual model, the basal lava flow overlying the basement rocks (LV001) was modeled as an aquitard.

Both the fine and coarse scale models were manually calibrated prior to MCMC sampling in order to achieve a relatively close fit between the model predictions and the measured natural state temperature data. This mainly involved manual adjustment of

**Table 1.** Assumed density and porosity (fixed) and prior means for permeability for the 14 rock units included in the numerical model.

| Rock type | Density (g cm$^{-2}$) | Porosity (-) | Cross-rift permeability ($k^x$, m$^2$) | Rift-parallel permeability ($k^y$, m$^2$) | Vertical permeability ($k^z$, m$^2$) |
|---|---|---|---|---|---|
| BASE1 | 2.75 | 0.05 | 7.5E-16 | 1.5E-15 | 1E-15 |
| BASE2 | 2.75 | 0.03 | 7.5E-16 | 7.5E-16 | 5E-16 |
| HY001 | 2.5 | 0.1 | 5E-14 | 1.5E-13 | 5E-14 |
| HY002 | 2.5 | 0.15 | 5E-14 | 1.5E-13 | 1.5E-13 |
| HY003 | 2.4 | 0.2 | 5E-14 | 1.5E-13 | 1E-13 |
| LV001 | 2.6 | 0.05 | 1E-16 | 2.5E-16 | 5E-17 |
| LV002 | 2.6 | 0.1 | 1E-13 | 2.25E-13 | 1.25E-13 |
| LV003 | 2.6 | 0.1 | 1E-13 | 2E-13 | 1E-13 |
| LV004 | 2.6 | 0.1 | 1E-13 | 2E-13 | 1.5E-13 |
| OUTER | 2.6 | 0.1 | 1E-15 | 1.5E-14 | 2E-15 |
| OUTBS | 2.75 | 0.05 | 5E-16 | 1E-15 | 7.5E-15 |
| BARFT | 2.6 | 0.1 | 2.5E-16 | 1E-15 | 1E-15 |
| TVFLT | 2.6 | 0.05 | 1.5E-15 | 7.5E-16 | 5E-15 |
| CLAYC | 2.6 | 0.2 | 2E-15 | 5E-15 | 5E-15 |

rock permeabilities and the distribution of heat and mass input at the base of the model, along with minor modifications made to the spatial configuration of the rock types. The anisotropic permeability of each rock unit along with other rock properties (density, porosity, thermal conductivity) achieved during the initial calibration are shown in Table 1. These values serve as the means of the prior probability distributions (assumed to be Gaussian with a fixed standard deviation of 0.75 log units) specified for the MCMC sampling.

The distribution of heat and mass input at the base of the model is shown in Figure 6. Heat flow was adjusted from 0.3 W m$^{-2}$ in the center of the caldera to 0.1 W m$^{-3}$ on the perimeter of the model, in accordance with estimates of regional heat flow values in Icelandic volcanic systems (Flóvenz & Saemundsson, 1993). The specific enthalpy of the input fluid is set to 3.2 MJ kg$^{-1}$, in accordance with measurements of the discharge enthalpy of the IDDP-1 well (Ingason et al., 2014). Temperature and pressure were not fixed at the base of the model. The total mass of high-enthalpy fluid added into the base of the system is 65.35 kg s$^{-1}$.

The inferred natural state temperature profiles used to calibrate the simulations were provided by Landsvirkjun in accordance with Iceland GeoSurvey (Mortensen et al., 2009; Weisenberger et al., 2015). Figure 7 shows an example of an inferred natural state temperature profile from measured downhole temperatures for well IDDP-1 (Mortensen et al., 2015). With increasing time subsequent to drilling, the measured temperatures more closely correspond to the inferred natural state temperature (black) as the well heats up. After the IDDP-1 well began to discharge, fluid with a temperature of 450 °C was eventually produced at the surface (Elders et al., 2011). This is not recorded in the downhole temperature data, due to the likelihood that the permeable zone in the near vic-

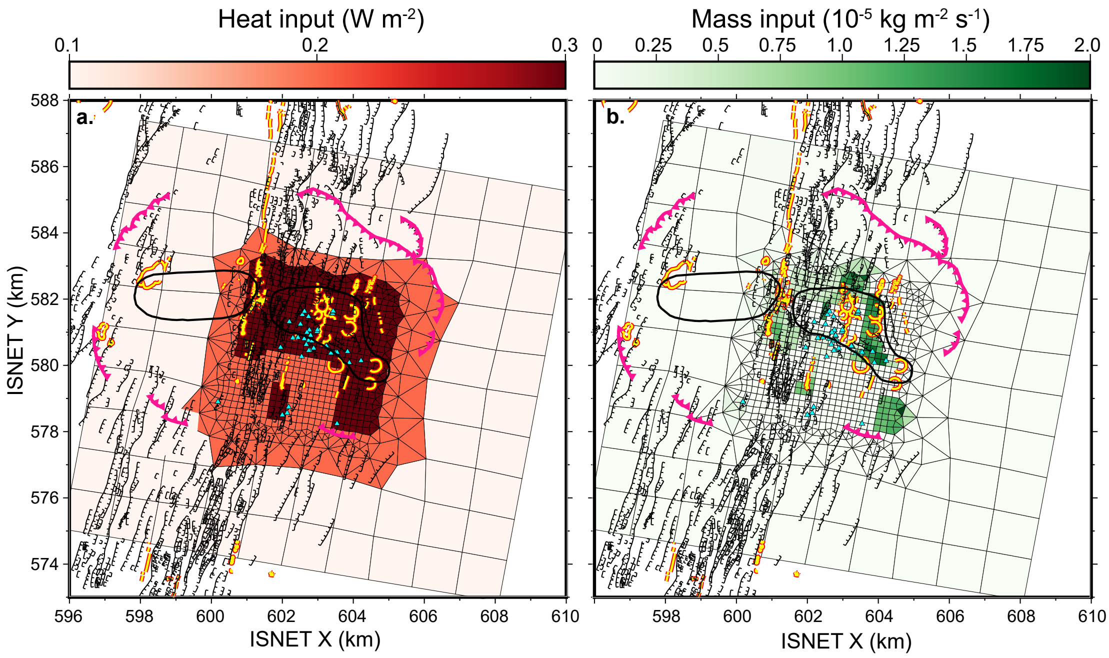


**Figure 6.** (a) Heat and (b) mass input into the base of the fine-scale model. The black lines show the boundaries of the zone with S-wave shadows detected by P. Einarsson (1978).

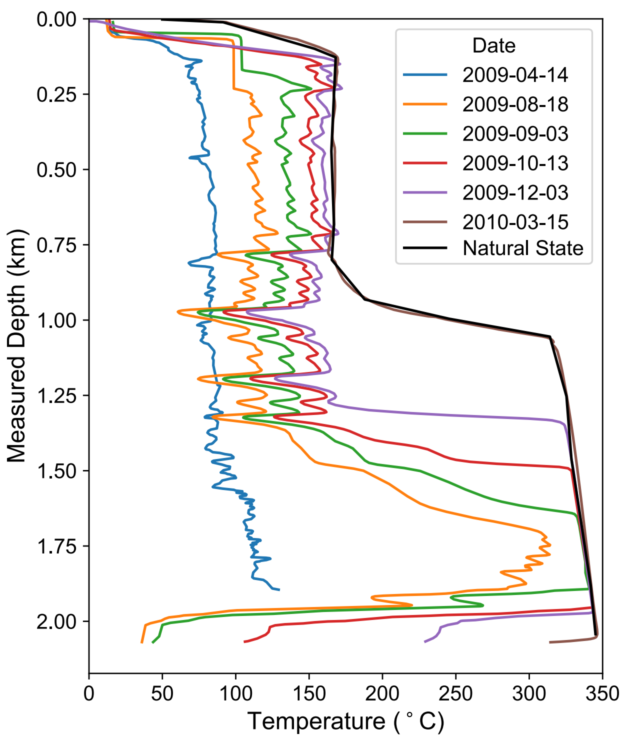


**Figure 7.** Measured temperatures between 2009-2011 during heating up of well IDDP-1 and comparison with inferred natural state temperature (black line).

inity of the intrusion was not finished heating up before a restriction in the casing of the well prevented downhole temperature logging (Axelsson et al., 2014).

### 3.2 Numerical Method

The simulations are carried out using AUTOUGH2 (Yeh et al., 2012), a version of TOUGH2 (Pruess et al., 2012) developed at the University of Auckland. The EOS3sc equation of state (EOS) (J. O'Sullivan et al., 2016, 2020), a modified version of the EOS1sc EOS (Croucher & O'Sullivan, 2008; Magnusdóttir & Finsterle, 2015), was used in order to extend the applicability of the model to the supercritical roots of the system. Although this EOS includes air and could in principle also model the vadose zone, the top of the model is set to the depth of the water table.

TOUGH2 solves the governing equations of mass and energy balance using a finite volume approach. For quantity $\kappa$ (e.g. energy $u$, mass $m$) within a finite volume $V_i$, bounded by a surface $\Omega_i$, conservation is represented in integral form as

$$\frac{\mathrm{d}}{\mathrm{d}t}\int_{V_i} M_\kappa \mathrm{d}V = -\int_{\Omega_i} \mathbf{F}_\kappa \cdot \mathbf{n}\mathrm{d}\Omega + \int_{V_i} q_\kappa \mathrm{d}V \tag{1}$$

where $t$ is time, $M_\kappa$ is mass or energy per unit volume (kg m$^{-3}$ or J m$^{-3}$, respectively), $F_\kappa$ is the flux of mass or energy, $q_\kappa$ represents sink and source terms (e.g. deep inflows), and $\mathbf{n}$ denotes an outward-pointing unit normal vector to the surface $\Omega_i$. The amount of mass ($M_m$) and energy ($M_u$) per unit control volume are given by

$$M_m = \Phi(\rho_l S_l + \rho_v S_v) \tag{2}$$

$$M_u = (1-\Phi)\rho_r u_r T + \Phi(\rho_l u_r S_l + \rho v u_v S_v) \tag{3}$$

where $\Phi$ is porosity, $S_\beta$ is the volumetric saturation of fluid phase $\beta$ (liquid $l$ or vapor $v$), $\rho_\beta$ and $\rho_r$ the density of the fluid phase or rock (denoted by subscript $r$), $u_\beta$ fluid phase internal energy, $u_r$ rock specific heat, and $T$ temperature. Fluid mass fluxes are described by a two-phase version of Darcy's law:

$$\mathbf{F}_\beta = -\mathbf{k}\frac{k_{r,\beta}}{\nu_\beta}(\nabla P - \rho_\beta \mathbf{g}) \tag{4}$$

where $\mathbf{k}$ is the permeability tensor (assumed to be diagonal), $\mathbf{g}$ the vector of gravitational acceleration, $P$ is pressure, and $k_\beta$ and $\nu_\beta$ are the relative permeability and kinematic viscosity of fluid phase $\beta$. Energy flux includes the contribution of heat conduction and advection of each fluid phase:

$$\mathbf{F}_u = -K\nabla T + \sum_\beta h_\beta \mathbf{F}_\beta \tag{5}$$

where $K$ is the effective thermal conductivity of the fluid-rock medium and $h_\beta$ is the specific enthalpy of fluid phase $\beta$.

TOUGH2 implements the integral finite difference method (Narasimhan & Witherspoon, 1976) for spatial discretization of the mass and energy conservation equations. A fully implicit scheme with adaptive time stepping is used for numerical integration in time, and upstream weighting of fluid properties is used for calculating flows between adjacent blocks. TOUGH2 uses the Newton-Raphson method and a preconditioned conjugate gradient sparse matrix solver to solve the system of equations (Pruess, 1991). Newton-Raphson iteration continues until the residual of the discretized version of the conservation equations are reduced to a small fraction of the mass accumulation terms, with the convergence criterion set to $1 \times 10^{-5}$. If convergence is not achieved within 9 iterations, the timestep is reduced by a factor of 5 and solution re-attempted; if convergence is achieved within 5 iterations, the next time-step is doubled. Once a steady-state natural state configuration is reached, time-steps increase up to a large value and the simulation runs to completion rapidly. We observed that convergence was not attained in some of the simulations, potentially as a result of convective instabilities in the upper high permeability rocks or grid blocks that change between phase regions in response to very small changes in pressure and temperature. Therefore, it was necessary to prematurely terminate simulations that take longer than 5 minutes to converge and not use them for calculation of the posterior statistics. However, this affected less than 5% of the simulations.

### 3.3 Bayesian Hierarchical Framework

According to the Bayesian framework, the solution to the inverse problem involving identification of geologically reasonable model parameters $\mathbf{k}$ consistent with measured data $\mathbf{y}_{\text{obs}}$ is a probability distribution calculated using Bayes' theorem, written schematically as:

$$p(\mathbf{k} \mid \mathbf{y}_{\text{obs}}) \propto p(\mathbf{y}_{\text{obs}} \mid \mathbf{k})p(\mathbf{k}) \tag{6}$$

Following standard terminology, $p(\mathbf{k} \mid \mathbf{y}_{\text{obs}})$ refers to the posterior, $p(\mathbf{y}_{\text{obs}} \mid \mathbf{k})$ the likelihood and $p(\mathbf{k})$ the prior. Bayes' theorem is written above as a proportionality relationship, omitting a normalization factor that is not required by most sampling algorithms (Gelman et al., 2013). For natural state geothermal reservoir models, the main adjustable model parameters include the spatial configuration of rock types, the anisotropic permeability of each rock type, and the locations and magnitudes of deep hot inflows. In this study, we limit the parameters of interest for uncertainty quantification to the anisotropic permeability of each rock type; the model geologic structure (Figure 4) as well as the locations and magnitudes of heat and mass input (Figure 6) are fixed. The observed data consist of inferred natural state temperatures from 40 deep geothermal wells (Figure 3), which were interpolated to layer centers in the coarse model, leading to 261 total observation points.

The main challenge associated with the application of Bayes' theorem to geothermal systems is the computational cost involved in the repeated evaluation of the forward model. While a significant speed-up can be achieved by using a coarsened version of the forward model in place of a finer, more accurate model, this introduces approximation errors that can lead to incorrect estimation of model parameters and their associated uncertainties (Kaipio & Somersalo, 2007). As described by Maclaren et al. (2020), the Bayesian hierarchical framework allows the resulting model approximation error to enter into the calculation of the likelihood as a probabilistic process error via decomposition of a full joint probability distribution over all quantities of interest into a measurement model, process model, and parameter model:

$$p(\mathbf{y}_{\text{obs}}, \mathbf{y}_{\text{process}}, \mathbf{k}) = p(\mathbf{y}_{\text{obs}} \mid \mathbf{y}_{\text{process}})p(\mathbf{y}_{\text{process}} \mid \mathbf{k})p(\mathbf{k}) \tag{7}$$

where the distribution parameters and distribution subscripts are suppressed for simplicity. The latent process vector is assumed to be generated by the fine-scale model

$$\mathbf{y}_{\text{process}} = f(\mathbf{k}) \tag{8}$$

The use of the coarsened model $g(\mathbf{k})$ in place of a finer, more accurate model $f(\mathbf{k})$ introduces additional approximation errors, which are defined as

$$\boldsymbol{\epsilon} = \mathbf{y}_{\text{process}} - g(\mathbf{k}) = f(\mathbf{k}) - g(\mathbf{k}) \tag{9}$$

Assuming additive error models (Maclaren et al., 2020), the measurement and process model components correspond to a two-stage decomposition of the form

$$\mathbf{y}_{\text{obs}} = \mathbf{y}_{\text{process}} + \mathbf{e} \tag{10}$$

$$\mathbf{y}_{\text{process}} = g(\mathbf{k}) + \boldsymbol{\epsilon} \tag{11}$$

where $\mathbf{e}$ is the measurement error (which may include correlations). Combining the approximation errors with the measurement errors to give the total error ($\nu = \mathbf{e} + \boldsymbol{\epsilon}$), the measurement model can be written as:

$$\mathbf{y}_{\text{obs}} = g(\mathbf{k}) + \epsilon + \mathbf{e} = g(\mathbf{k}) + \boldsymbol{\nu} \tag{12}$$

Obtaining the likelihood $p(\mathbf{y}_{\text{process}} \mid \mathbf{k})$ using these functional relationships is done by marginalizing over the total error, assuming that the measurement and approximation errors are independent of the parameter vector (Maclaren et al., 2020), so that:

$$p_{Y_0|K}(\mathbf{y}_{\text{obs}} \mid \mathbf{k}) = p_{\boldsymbol{\nu}}(\mathbf{y}_{\text{obs}} - g(\mathbf{k})) \tag{13}$$

Then, the posterior can be written as

$$\begin{aligned} p_{K|Y_0}(\mathbf{k} \mid \mathbf{y}_{\text{obs}}) &\propto p_{Y_0|K}(\mathbf{y}_{\text{obs}} \mid \mathbf{k}) p_K(\mathbf{k}) \\ &= p_{\boldsymbol{\nu}}(\mathbf{y}_{\text{obs}} - g(\mathbf{k})) p_K(\mathbf{k}) \end{aligned} \tag{14}$$

where the process error is absorbed into the likelihood.

Absorbing the process error into the likelihood in this manner requires the distribution of the total error, $p_{\boldsymbol{\nu}}(\cdot)$, to be known. In standard Bayesian approximation error approaches, the statistics of the model approximation errors are precomputed empirically by drawing samples from the prior distribution. However, sampling from an insufficiently informative prior and running the fine-scale geothermal reservoir model leads to a high probability of practical issues such as model run failures, long model run times, and/or extreme model inputs. Therefore, Maclaren et al. (2020) developed the posterior-informed composite approximation error approach, where the statistics of the model approximation error are obtained via direct sampling from a *naïve posterior* computed by separate MCMC sampling using the coarse model without consideration of any approximation errors. Thus, the model approximation error is made using a posterior plug-in estimation where the coarse model posterior is used to estimate the error distribution marginalized over the parameter:

$$p_\epsilon(\epsilon) \leftarrow \hat{p}_{\epsilon|Y_o}(\epsilon \mid \mathbf{y}_{obs}) = \int p_{\epsilon|K}(\epsilon \mid \mathbf{k}) \hat{p}_{K|Y_o}(\mathbf{k} \mid \mathbf{y}_{obs}) \mathrm{d}\mathbf{k} \tag{15}$$

where the likelihood function in $\hat{p}_{K|Y_o}$ is based on the coarse-scale model $g(\mathbf{k})$ without accounting for approximation errors. Once the error distribution has been estimated, the composite model of the joint distribution along with the original prior is used:

$$p_{\epsilon,K}(\epsilon, \mathbf{k}) \leftarrow p_\epsilon(\epsilon) p_k(\mathbf{k}) \tag{16}$$

Although the use of the naïve posterior for calculating of the model approximation error may narrow the error distribution when compared to the distribution that results from the prior, it has the benefit of providing more relevant estimates of the model error when the posterior based on the coarse model is not too far from the true posterior, which is the case for our models.

In this study, the statistics of the approximation error were calculated by drawing an ensemble of $q = 150$ samples from the naive posterior density $\hat{\mathbf{p}}(\mathbf{k} \mid \mathbf{y}_{obs})$ with $\mathbf{k}^\ell$ for $\ell = 1, 2, ..., q$. Assuming the the approximation error is Gaussian, its distribution can be calculated from the ensemble mean and covariance:

$$\epsilon_* = \frac{1}{q} \sum_{\ell=1}^{q} \epsilon^{(\ell)}, \quad \Gamma_\epsilon = \frac{1}{q-1} \sum_{\ell=1}^{q} (\epsilon^{(\ell)} - \epsilon_*)(\epsilon^{(\ell)} - \epsilon_*)^T \tag{17}$$

As the total error $\nu$ is the sum of both the noise and the approximation error, given the normality assumption, the distribution of the total error is given by:

$$\nu \sim \mathcal{N}(\nu_*, \Gamma_\nu) = \mathcal{N}(\mathbf{e}_* + \epsilon_*, \Gamma_e + \Gamma_\epsilon) \tag{18}$$

This enters into the likelihood as follows:

$$p_\nu(\mathbf{y}_{\text{obs}} - g(\mathbf{k})) \propto \exp\left(-\frac{1}{2}\sum_{i=1}^{N}(g^N(\mathbf{k}) - \nu_*^N - \mathbf{y}_{obs}^N)^T\Gamma_\nu^{-1}(g^N(\mathbf{k}) - \nu_*^N - \mathbf{y}_{obs}^N)\right) \tag{19}$$

In our simulations, we observe that the covariance of the approximation errors differs greatly for different measurements; namely, the approximation errors for temperature measurements in the liquid isothermal zone show a high covariance, and the approximation errors for temperature measurements in the boiling zones show low covariance. This influences the relative weight of the residual of these measurements on the likelihood, increasing the importance of the temperature measurements where a larger covariance is calculated by the approximation error model. Therefore, to avoid this, we also perform MCMC sampling using a likelihood function that only considers the means of the approximation errors (i.e. offset or bias term) and a constant noise term:

$$p_\nu(\mathbf{y}_{\text{obs}} - g(\mathbf{k})) \propto \exp\left(-\frac{1}{2}\sum_{i=1}^{N}\frac{[g^N(\mathbf{k}) - \nu_*^N - \mathbf{y}_{obs}^N]^2}{\sigma^2}\right) \tag{20}$$

where the covariance of the temperature measurements is fixed (i.e. $\sigma^2 = 10$ ℃).

### 3.4 MCMC Sampling

Markov chain Monte Carlo (MCMC) sampling is carried out using the Python Package *emcee* (Foreman-Mackey et al., 2013), which implements an affine invariant ensemble sampler (Goodman & Weare, 2010). The *emcee* package implements the Stretch Move algorithm (Goodman & Weare, 2010), which is similar in principle to the standard Metropolis-Hastings algorithm (Metropolis et al., 1953), with a proposal and an accept/reject step. However, this method involves simultaneously evolving an ensemble of walkers, where the proposal distribution for one walker is based on the current positions of the other walkers in the complementary ensemble. Used in the context of our models, "position" refers to a vector in the 42-dimensional parameter space (the $x$, $y$, and $z$ permeabilities for the 14 different rock types). The property of affine invariance implies that the performance of the algorithm is independent of the aspect ratio in highly anisotropic distributions and is well-suited for skewed posterior distributions (Goodman & Weare, 2010).

The PyTOUGH library (Croucher, 2011; J. O'Sullivan et al., 2015) is used to interface the *emcee* sampler with the AUTOUGH2 simulator. For determination of both the 'naive' posterior and the discrepancy-informed posterior, 80,000 samples were computed (10 ensembles of 100 walkers taking 80 samples each). A total of 40,000 samples (4000 for each ensemble, 40 for each walker) were discarded as burn-in based on when the samples began to converge around a posterior certain probability (Fig 8a). The statistics of the model error were computed by running 150 iterations of the fine and coarse model using the statistics of the 'naive' posterior; this required approximately 15 days of computing time. All computations were carried out on a standard desktop computer with an Intel Xeon E5-1620 3.50 GHz 8-core processor. Each simulation using the coarse model took anywhere from 10 seconds to one hour to run; as noted above, in order to limit the computing time, coarse models that took longer than 5 minutes to run (less than 5% of all simulations) were terminated and not used for the calculation of posterior statistics. Each ensemble of 100 walkers took approximately $1.3\times10^6$ seconds (15 days) to run to completion. Since each simulation using the fine model took up 30 minutes - 1 day to run or more to run, MCMC sampling with an equivalently long chain and using the fine model would take more than year. Thus, this represents a significant speed-up and emphasizes the fact that the MCMC computations are only feasible using the coarse model.

The evolution of the posterior probability of the computed models is shown in Fig 8a, with the position of each walker at each iteration shown as a marker. Each walker

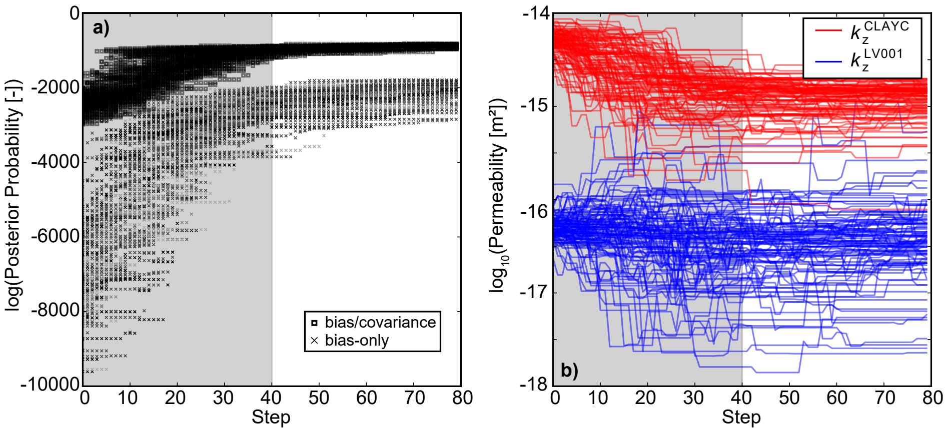


**Figure 8.** Trace of the log posterior probability function and two parameters during MCMC sampling. The first forty steps were discarded as burn-in (grey shaded area). a) Trace of the posterior probability showing the positions of walkers during successive steps. Samples in MCMC chains in which the likelihood function considers the bias and covariance or the bias-only of the approximation error and shown as rectangles and crosses, respectively. b) Trace of the vertical permeability of LV001 (blue lines) and the vertical permeability of the clay cap (red lines).

was initialized at a point in the parameter space in the near vicinity of the prior means for each parameter (Table 1). The example parameter trace for the vertical permeability of LV001 (blue line in Fig 8b) show that the walkers tend to cluster around the prior mean, which is the case for many of parameters. However, the trace of the vertical permeability of the clay cap (red line in Fig. 8b) shows that the inversion process results in walkers tending towards lower permeability values. The acceptance fraction varied between the chains from $\leq 0.05$ to 0.5, with an average of 0.26, close to the optimal range (Gelman et al., 1996).

The correspondence between the prior and posterior means could be the result of a highly informative prior model, but could also result from autocorrelation. Convergence tests such as the autocorrelation time indicate that the chain is not long enough (Foreman-Mackey et al., 2013), and an insufficient number of independent samples were obtained to ensure representative sampling of the target density. However, due to practical limitations imposed by the relatively long amount of time required to run the AUTOUGH2 forward models, which were run in serial and sequentially, it is not presently feasible to run a chain long enough to ensure convergence to the target posterior. Despite this obvious shortcoming, we simply note that this approach allows for practical uncertainty quantification of inferred rock permeabilities, assuming that the prior model is highly informative, a necessary assumption when applying inverse modeling tools for natural state geothermal reservoir model calibration (M. O'Sullivan & O'Sullivan, 2016).

## 4 Results

The Bayesian calibration scheme improves the fit between the model results and the inferred natural state temperature profiles. Systematically different posterior results are achieved if the MCMC sampling is carried out using the coarse model without any approximation error model (the naïve posterior), or with an approximation error corrected model. The approximation error model can account for the bias of approximation errors (the mean offset between the fine and coarse models) (Eqn. 20) or both the bias and covariance of the approximation errors (Eqn. 19). Posterior predictive checks compare the data generated using the fitted model with the observed data (Gelman & Hill, 2006), show the ability of the stochastic model to match the inferred natural state temperature distribution. Although MCMC sampling is performed using the coarse model, all posterior predictive checks are computed using the fine model with parameter sets from the respective posterior (naive, bias-only, or bias/covariance). The posterior probability distribution functions (pdfs) of the anisotropic permeability of the 14 different rock types quantify the uncertainty underlying their estimation.

### 4.1 Posterior predictive checks

The modeled natural state temperature distribution generally corresponds well to the inferred natural state temperature field. Figure 9 compares model predictions with measured data (posterior predictive checks) for 8 wells located in the Leirbotnar subfield. Compared to the fine model assuming prior means for all parameters (dashed blue lines in Figs. 9-11), posterior results achieve a closer fit to the inferred natural state temperature data (black lines). These temperature profiles reproduce the characteristic temperature-depth relationship in Leirbotnar, with the upper isothermal zone at temperatures ∼180-220 ℃ underlain by a deeper boiling reservoir.

Several of the wells (Figure 9a-d) show a good correspondence between the mean temperature of the isothermal zone computed by the set of posterior predictive samples and the inferred natural state temperatures. However, the models predict 20-40 ℃ higher temperatures in the isothermal zone than measured for several wells. Only considering the bias in the approximation error model (orange lines in Fig. 9-11) results in a closer approach to the inferred temperature of the isothermal zone than if both the bias/covariance of the approximation errors are considered (blue lines in Fig. 9-11). Posterior samples from the latter tend to systematically show temperatures 20-40 ℃ higher than inferred. The model clearly reproduces the transition between the upper near-isothermal liquid aquifer and deeper boiling aquifer, but the model results for wells KG-08, KG-24 and KW-02 show this transition occurring at shallower depths than measured. The uncertainty in posterior temperature is larger in the isothermal zone and at depths ≤-2 km a.s.l. than in the near surface (≥ 0 km a.s.l.) or between 1-2 km b.s.l. This is at least partially a result of the fact that temperatures in boiling zones following the boiling point with depth, and are dependent mainly on the hydrostatic pressure.

Figure 10 shows posterior predictive checks for selected wells located in the Suðurhlíðar subfield, The model clearly reproduces the vertically-extensive boiling zone between the surface and -2 km a.s.l. in Suðurhlíðar. Due to the thermodynamic constraint imposed by the co-dependence of temperature and pressure at boiling conditions, the uncertainty in in temperatures in model predictions in boiling zones is low. The greatest uncertainty in model predictions is at depths ≤ -1.5 km a.s.l., below the maximum depth of the drilled wells, where the posterior predictive samples shows temperatures ranging between 200-400 ≥ ℃ (e.g. Fig. 10e). Temperatures in excess of the critical temperature of pure water (≥374 ℃) are predicted below -2 km a.s.l. in several wells (KJ-31, KJ-37). However, in other wells (KJ-19, KJ-39, KJ-36) the model suggests the potential for significant deep temperature inversions below -1.5 km a.s.l. A temperature inversion below -0.5 km asl measured in well KJ-17 is generally reproduced by the model (Fig. 10g), but there is significant uncertainty in the depth and magnitude of the temperature reversal. The model does not reproduce the lower temperatures closer to the surface in well KJ-14 (Fig 10f).

Figure 11 shows posterior predictive checks for 3 wells located in the Hvíthólar subfield as well some other wells on the margin or away from the main production field. The model clearly reproduces the temperature inversion between -0.5 km a.s.l. as well as the slight increase in temperature beneath -1 km a.s.l. in wells KJ-22 and KJ-23, although the model tends to suggest a more rapid decrease in temperature with increasing depth below 0 km a.s.l. There are certain wells that the model does poorly at reproducing mea-

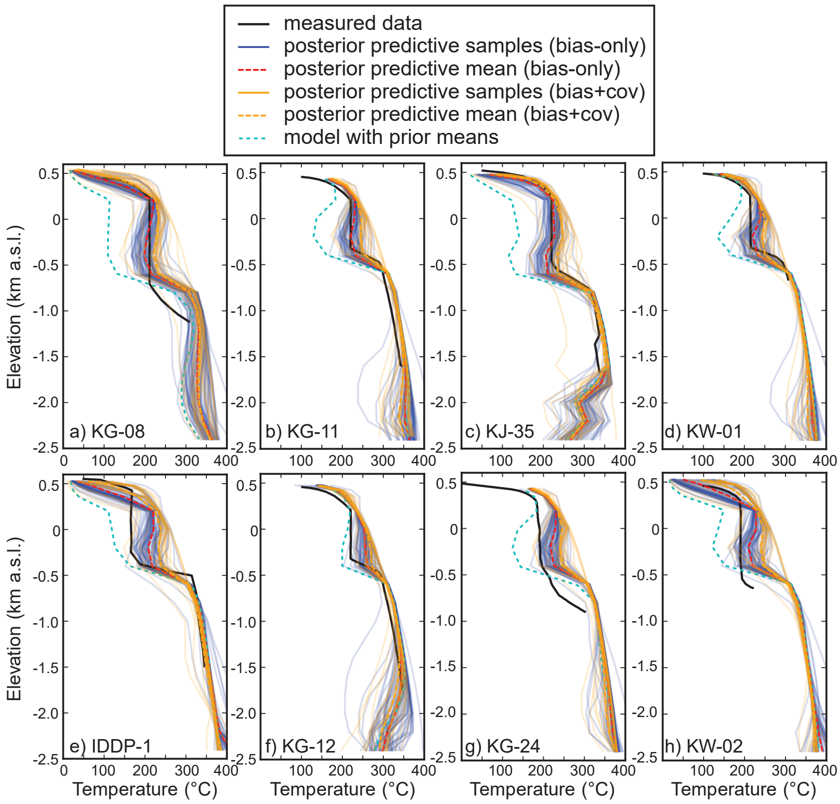


**Figure 9.** Posterior predictive checks for Leirbotnar wells a) KG-08, b) KG-11, c) KJ-35, d) KW-01, e) IDDP-1, f) KG-12, g)KG-24, h) KW-02. Posterior predictive samples generated using the bias-only correction in the approximation error model are shown in blue (with the mean of the subset of posterior samples is shown with a red dashed line), and posterior predictive samples generated with an approximation error model considering both the bias and covariance are shown in orange, (with the mean as an orange dashed line). The inferred natural state temperatures are shown in black. Temperatures calculated assuming prior means for all parameters are shown with the dashed blue line.

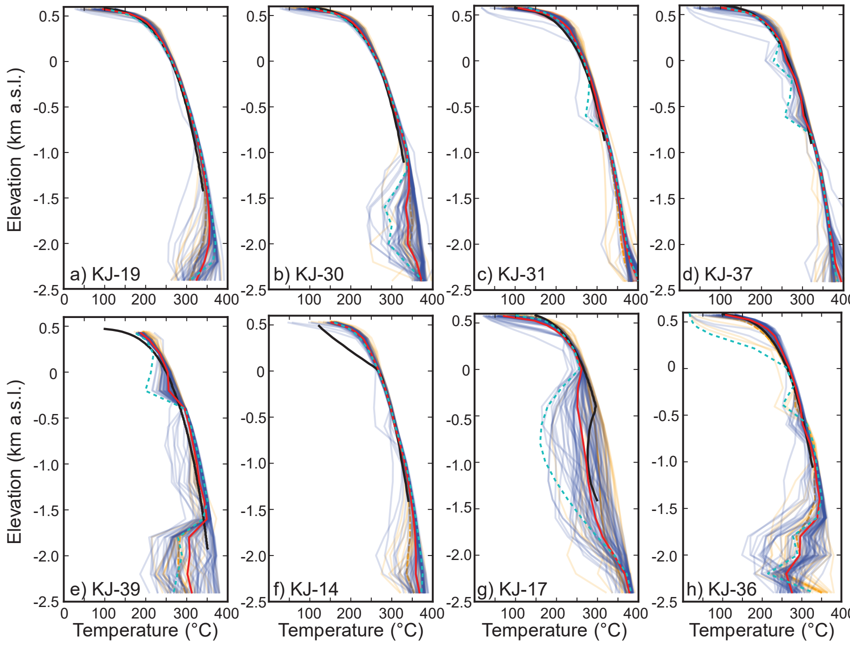


**Figure 10.** Posterior predictive checks for Suðurhlíðar wells a) KJ-19, b) KJ-30, c) KJ-30, d) KJ-37, e) KJ-39, f) KJ-14, g) KJ-17, and h) KJ-36 in Vesturhlíðar. Symbology same as in Fig. 9.

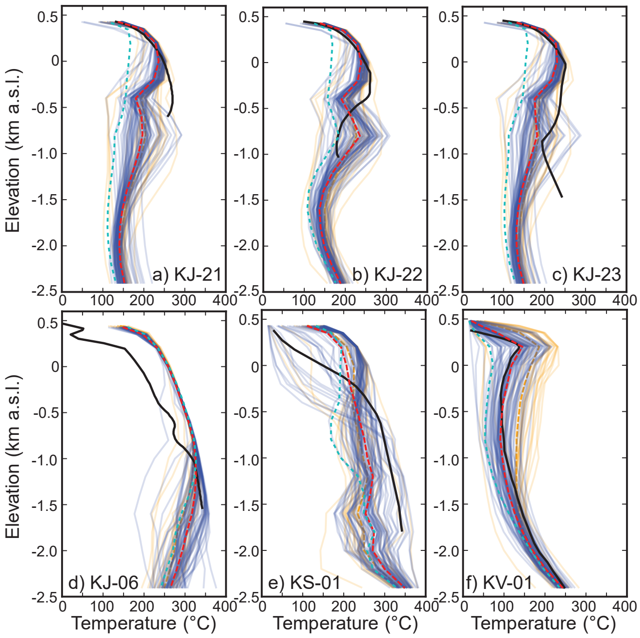


**Figure 11.** Posterior predictive checks for Hvíthólar wells a) KJ-21, b) KJ-22, c) KJ-23, as well as d) KJ-06, e) KS-01, f) KV-01. Symbology same as in Fig. 9.

sured temperatures. For example, the model fails to reproduce the strong temperature decrease above -1 km a.s.l. in KJ-06, located at the southern margin of Leirbotnar (Fig. 11d). Similarly, the model does not reproduce the near linear temperature gradient in the upper 1 km in well KS-01 (Fig. 11e). The model closely matches the measured temperatures in well KV-01 (Fig. 11f), which is located at the periphery of the production area and shows low temperatures $\leq$ 200 °C to 2 km depth, suggests that the model is broadly capturing the temperature distribution of the groundwater system outside of the main production field.

### 4.2 Posterior Parameter Distributions

The uncertain parameters in this model consist of anisotropic permeabilities for 14 different rock types. Figure 12 shows the marginal posterior densities for 4 different rock types (BASE1, OUTER, HY001, CLAYC) for each direction (x = cross-rift, y = rift-parallel, z = vertical). This figure compares posterior pdfs corresponding to the naive (blue line) and the discrepancy-informed models, either considering both the bias and covariance terms in the approximation error (orange) or the bias-only (red lines).

Compared to the prior uncertainty (dashed blue lines), which extends over four orders of magnitude, Figure 12 indicates that the MCMC process reduces uncertainty in the inferred permeability values. The naïve and discrepancy-informed models reach fairly consistent results, with a Gaussian-looking pdf often centered on or near the prior means. Generally, many of the parameters show substantial uncertainty, with posterior densities extending over 1-2 orders of magnitude or more. The uncertainty in parameter values is higher in the discrepancy-informed model compared to the naïve model, particularly if both the bias and covariance of the approximation errors are considered. In the latter case, the boundaries of the prior seem to exercise some control on the limits of the posterior uncertainty (e.g. Figure 12e,f).

Although there is a clear correspondence between the mode of the posterior and the prior means, the high posterior uncertainty of many of the parameters suggests limited identiability. However, certain parameters show narrower posterior distributions centered at an offset from the prior mean, This includes the particularly the vertical permeability of the clay cap (Fig. 12l). Thus, this appears to be one of the most strongly identifiable parameters, with a maximum *a posteriori* value narrowly focused around $\sim 10^{-15}$ m$^2$.

The posterior pdfs indicate significant permeability anisotropy, particularly for the upper extrusive rock types (hyaloclastites and lava flows) and the fault rock types. Figure 13a-b compares the posterior densities (computed using the approximation error model considering the bias-only correction) in different orientations for the permeability of hyaloclastites (3 units), lava flows (4 stratigraphic units), Generally, with the exception of LV001 (which is modeled as an aquiclude), the predicted permeability of the hyaloclastites and lava flows is very high ($10^{-14}$ - $10^{-12}$ m$^2$). For both the hyaloclastites and lava flows (Fig. 13a,b), the rift-parallel permeability (red lines) seems to be higher ($10^{-13}$ m$^2$ than the cross-rift (grey lines) or vertical (blue lines) permeability. The predicted permeability of the lowermost lava flow LV001 is distinctly lower ($10^{-17}$ - $10^{-15}$ m$^2$).

Figure 13c shows that the fault rock types (barrier faults, shown by the solid lines, and transform fault, shown by the dashed lines) show distinct anisotropic permeability contrasts consistent with their strikes. The barrier faults (solid lines), which strike SW-NE parallel to the rift, show intermediate rift-parallel (x) and vertical permeability (z) around $10^{-15}$ m$^2$, but lower cross-rift permeability ($\sim 10^{-16}$ m$^2$). The NNW-SSE-striking transverse faults (dashed lines) oriented roughly perpendicular to the axis of rifting, show intermediate rift-parallel permeability but higher cross-rift and particularly vertical permeability ($10^{-15}$ m$^2$). These results indicate that these the faults are generally more permeable along the axis of their strike, retain moderate vertical permeability, and are less permeable across strike.

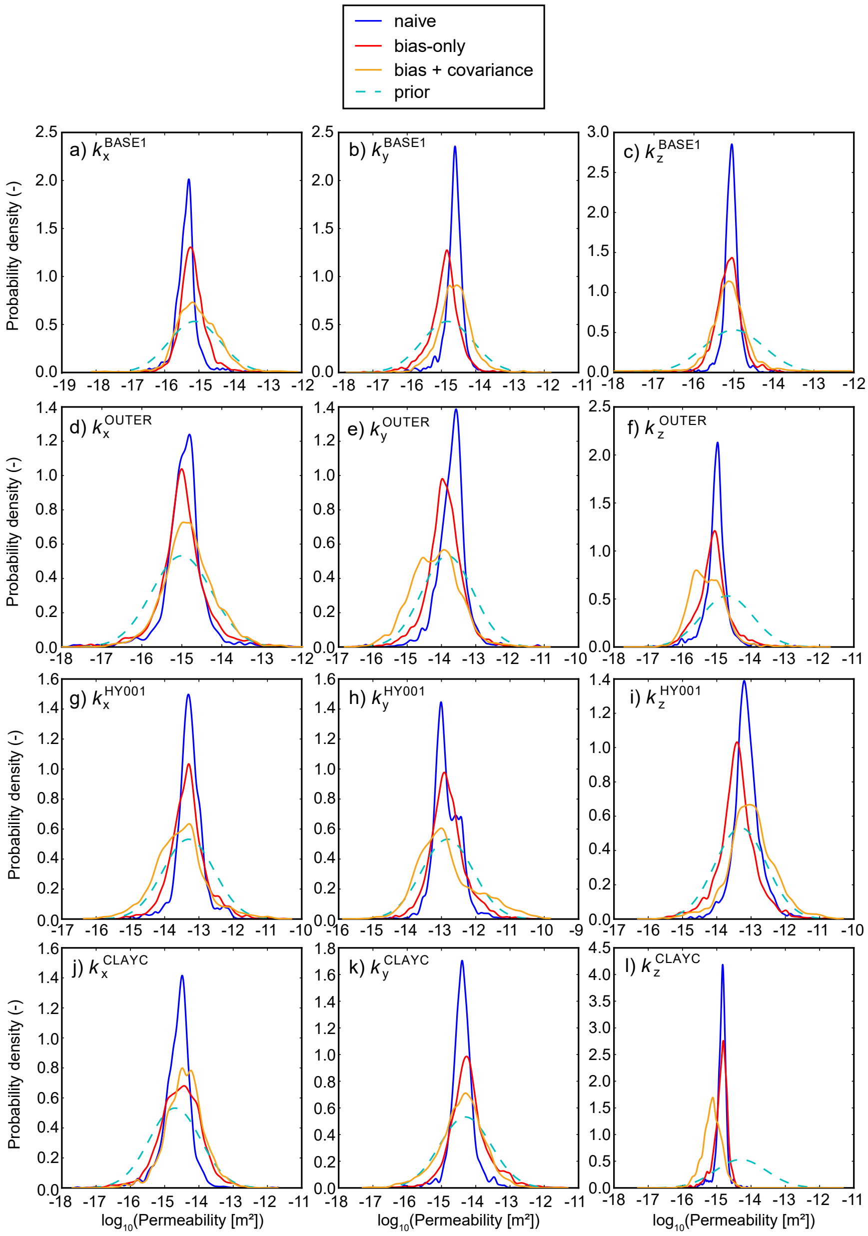


**Figure 12.** Marginal posteriors for permeability (x = cross-rift, y = rift-parallel, and z = vertical) for four rock types, a-c) BASE1, d-f) OUTER, g-i) HY001, j-l) CLAYC. The blue lines shows the naïve posterior, calculated by performing MCMC on the coarse model without any approximation error. The dashed light blue lines shows the prior. The solid red lines shows the posterior calculated by the discrepancy-informed model with bias-only correction to the likelihood function. The orange line shows the posterior calculated by the discrepancy-informed model considering both the bias and covariance in the model approximation error.

# 5 Discussion

## 5.1 Calibration of natural state reservoir models

We have presented an approach to inverse modeling of geothermal reservoirs that incorporates the additional error resulting from performing MCMC sampling with a "coarse",

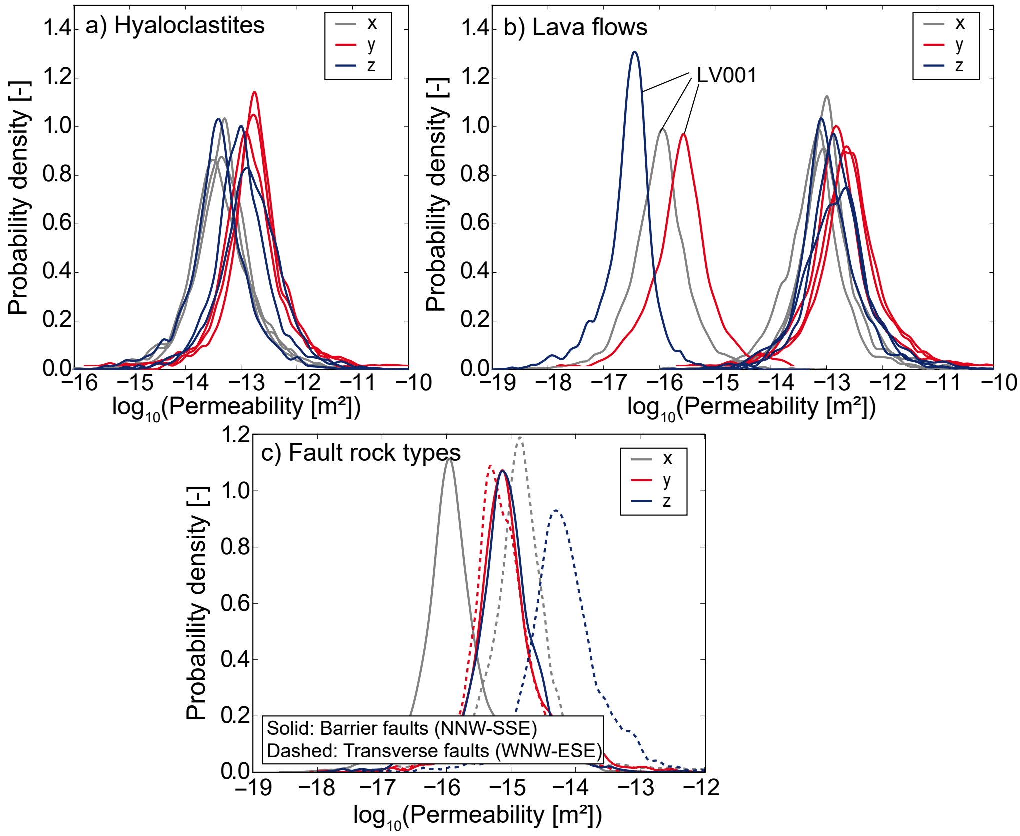


**Figure 13.** Marginal posterior densities for permeability in different directions (x = cross-rift, shown with grey lines, y = rift-parallel, shown with red lines, and z = vertical, shown with dark blue lines) for a) Hyaloclastites (HY001, HY002, HY003) b) Lava flows (LV001, LV002, LV003, LV004) c) Fault rock types (barrier faults, BARFT, shown as solid lines, and transform faults, TVFLT, shown as dashed lines).

relatively inexpensive model instead of a finer, computationally expensive model into a hierarchical Bayesian framework. Compared to other approaches that construct approximate posterior distributions using reduced-order models in the context of natural state geothermal reservoir models, such as delayed acceptance schemes that calculate the model reduction error dynamically (Cui et al., 2011; Cui, Fox, & O'Sullivan, 2019; Cui, Fox, Nicholls, & O'Sullivan, 2019), the approach of Maclaren et al. (2020) is relatively easy to implement, requiring a relatively small number of fine model simulations to construct the posterior-informed model approximation error. Despite a huge reduction in the dimensionality of the coarse model compared to the fine model (from 17193 to 2551 grid blocks), the naïve posterior is strongly informative (Fig. 12), suggesting that the physics of the fine model are adequately captured in the coarse model and that the approximation error calculated using the naïve posterior yields relevant error estimates.

Despite the computational intensity involved with running hundreds of thousands of AUTOUGH2 models, the MCMC approach can be used to achieve a reasonably good fit to temperature data derived from 40 deep geothermal wells. Such a fit has also been obtained for large-scale reservoir models using manual calibration (Ratouis et al., 2016) or optimization based schemes such as iTOUGH2 and PEST (Mannington et al., 2004; Gunnarsson et al., 2010; Prasetyo et al., 2016). However, it is not uncommon that optimum inferred parameter values differ greatly from initial "best-guess" estimates, or are restricted by reasonable bounds imposed on the inversion process (Reid & Wellmann, 2012; Kondo et al., 2017). While iTOUGH can be useful for showing the most uncertain parameters (Moon et al., 2014), when an optimization function can have several local minima, as is likely for geothermal data, the algorithms often only converge to the minima closest to the initial starting guess (Plasencia et al., 2014).

The data (downhole temperature profiles) and parameter (posterior parameter distributions) space show considerable differences arising if the likelihood function is induced by both the bias and covariance of the model approximation errors or the bias-only. This results from the much higher covariance of certain model approximation errors for certain measurements, particularly for measurement points in the isothermal zone, effectively resulting in a lower weight for these measurements in the likelihood function. In contrast, the covariance of model approximation errors in the boiling zones is very low due to the boiling point with depth constraint. Therefore, we suggest the use of a bias-only correction can be justified in such cases where the variability of coarse and fine model results is much greater in selected measurement points.

This study shows that a Bayesian framework to calibrate natural state geothermal reservoir models allows quantification of the uncertainty of the inferred permeability structure while retaining strong prior beliefs about the geologic/hydrologic structure of the system. Although the anisotropic permeability of each rock type are treated as stochastic parameters, the arrangement of rock types and the applied mass and heat fluxes at the base of the model are fixed. Other studies have also treated the input mass as an uncertain variable during calibration and even treated each block as a separate rock type (Cui et al., 2011). However, in our case this would result in a very large dimensional parameter space that would limit the feasibility of using the affine invariant MCMC sampling scheme (Foreman-Mackey et al., 2013). Rather, our approach ensures a close link between the conceptual model and the reservoir model, in effect allowing the reservoir model to serve as a test of the conceptual model. The relatively good match between measured data and simulation results may suggest that the conceptual model is highly informative. Moreover, the general correspondence between the prior and posterior means for permeability suggests that the *a priori* permeability ranges for the different rock types are realistic.

Inferred permeabilities in the range of $10^{-16}$-$10^{-12}$ m$^2$ are consistent with previous field measurements in geothermal systems (G. Björnsson & Bödvarsson, 1990; Ingebritsen & Manning, 2010). Although permeabilities measured in intact core samples under confining pressures are lower than inferred in this study (Eggertsson, Lavallée, et al., 2020;

Eggertsson, Kendrick, et al., 2020; Weaver et al., 2020), this discrepancy can generally be explained as permeability being fracture-controlled (Lamur et al., 2017). For a geothermal field such as Krafla, such fine-scale permeability heterogeneities will not be captured in models that assume permeability is fixed for each rock type or within grid blocks of the resolution used in this study. Previous modeling studies of Icelandic geothermal systems have inferred similarly high permeability values for extrusive volcanic rocks (hyaloclastites and lava flows). For example, using drawdown (pressure) and tracer data, Aradóttir et al. (2012) calculated lateral and vertical permeabilities of $3\times10^{-13}$ and $1.7\times10^{-12}$ m$^2$ for the basaltic lava flows hosting the Carbfix injection site at the Hellisheidi geothermal field. These values lie at the high end of the inferred permeability values in this study (Fig. 13a,b).

The inferred permeability values of the different rock types reflect the conceptual model. If a different conceptual model was assumed, with a significantly different geologic structure and distribution of heat and mass at the bottom boundary, different calibrated rock permeabilities would result. For example, tests were carried out to investigate results if the prior permeability of the aquitard (LV001) was set to be similar the other hyaloclastites and lava flows. Given this scenario, the model resulted in much higher natural state temperatures in the isothermal zone than measured, unless the prior permeability of the extrusive volcanic rocks was unrealistically high ($\geq10^{-11}$ m$^2$). Such high rock permeabilities are not justified by the data cited above. Given the inherent uncertainty of the conceptual model and data, a range of different conceptual models should be developed and tested using numerical models (Cumming, 2016b). Bayesian approaches are well-suited to incorporate future conceptual model reassessments and additional constraints as new geologic and thermohydrodynamic data becomes available.

This study shows several practical limitations to using MCMC sampling for inverse modeling of the natural state of geothermal reservoirs. Running a single ensemble of 100 MCMC walkers for 80 steps required computational time in excess of two weeks. In addition, computation of the approximation error model and the posterior predictive checks required significant computational expense, as a single fine model iteration could take up to a day or more to compute. More troublingly, the integrated autocorrelation time suggests that the chain is not long enough and adequate coverage of the target posterior density is not ensured. While running 1000+ iterations in each chain wasn't possible in the present study due to time constraints, ongoing efforts to parallelize TOUGH2 may enable this in the future (J. O'Sullivan et al., 2019; Croucher et al., 2020). Another possible indication of inadequate uncertainty is the observation that limits of the prior pdfs for permeability coincide with the limits of the posterior uncertainty (e.g. Fig. 12g-i). However, widening the prior further would have the disadvantage that the chain would take a significantly longer time to run, without necessarily providing more realistic estimates. Thus, the prior means and bounds must be carefully selected based on consideration of realistic permeability ranges observed in similar types of geothermal systems. Although MCMC methods may be prone to underestimating uncertainty due to the effects of autocorrelation and an insufficiently broad prior, the value of the calibrated permeabilities and uncertainty metrics ultimately hinges on the conceptual model and the assumption of an informative prior model. This will inevitably be the case for natural state geothermal reservoir models, which are poorly suited to "black box" inverse modeling approaches. In addition, the reliability of the inferred permeability structure depends greatly on the quality of data (both geologic and downhole measurements) used to calibrate the numerical model. Given the limited temperature data at depth $\geq$2 km, the uncertainty of the model predictions in the "deep roots" of the system is much greater than at shallower depths, as is reflected by the posterior predictive checks (Figs. 9-11).

### 5.2 The natural state of the Krafla geothermal reservoir

The foundation of the natural state geothermal reservoir model presented in this study is the conceptual model described in Section 2.2. According to our conceptual model, the distinctive spatial variability of temperature in Krafla is the combined result of heterogeneous upflow of high-enthalpy fluid from the deep heat source, structural partitioning of the reservoir by the Hveragil eruptive fissure, and the presence of a low permeability aquitard isolating the shallow boiling zone in Leirbotnar from the deeper boiling zone. Superimposed on these factors is the effect of topography-driven fluid flow associated with the Mt. Krafla, which shields the Suðurhlíðar system from intensive cold recharge leads to the relatively low temperatures in Leirbotnar.

Model results derived from the *maximum a posteriori* (MAP) estimate are presented in Figure 14 with the same cross-sections used to develop the conceptual model. Schematic flow arrows in Figure 14a indicate intensive southward-directed recharge into Leirbotnar at the depth of the isothermal zone (-0.5 km a.s.l.). Similarly intensive lateral recharge is lacking in the Suðurhlíðar subfield, likely due to the topographic high associated with Mt. Krafla, which leads to higher hydrostatic pressures in this area. Increasing temperatures within the isothermal zone to the SE of Leirbotnar result from increased mixing of ascending fluid within the Hveragil fault to the SW. Thus, the model predicts that topographic gradient from the NE to the SW drives fluid flow to the SW, resulting in cooling of the Leirbotnar isothermal zone as well as the shallow outflow in Hvítholar.

As a result of intensive cold water recharge from the north in the Leirbotnar area, boiling is confined to depths $\leq$-0.5 km. However, boiling extends to the surface in the Suðurhlíðar area ( Fig. 14b). The distribution of boiling zones is supported by the temperature measurements as well as production data. Wells that produce exclusively from the upper reservoir in Leirbotnar have enthalpies 0.8-1 MJ $kg^{-1}$, indicative of a single-phase liquid reservoir. In contrast, wells that produce from the deeper reservoir in Leirbotnar or in Suðurhlíðar develop much higher discharge enthalpies (up to $\sim$2.7 MJ $kg^{-1}$, corresponding to the specific enthalpy of saturated vapor), indicative of a boiling reservoir (Guðmundsson & Arnórsson, 2002).

Zones of single-phase vapor develop beneath Suðurhlíðar, Vestursvaedi, and the northern part of Leirbotnar $\leq$-2 km a.s.l. (Fig. 14b,c,d) Generally, the models predict single-phase vapor zones at greater depths and lower temperatures than experienced during the drilling of the IDDP-1 well, which discharged a ca. 440 ℃ vapor with an enthalpy of 3.2 MJ kg $^{-1}$ (Axelsson et al., 2014). However, as the role of the heat source is represented using boundary conditions, the structure of the vapor zones is controlled by the input of high-enthalpy fluid at the bottom boundary (Fig. 6b). Reproducing the rapid temperature in the proximity of shallow intrusions like those encountered during the drilling of IDDP-1 and KJ-39 requires explicit representation of fluid flow around intrusions (Scott et al., 2015). Despite this limitation, the models show how zones of supercritical fluid form at depth in the Krafla system and undergo ascent and decompression to form overlying boiling zones. The flow arrows at the base of the model in Fig. 14 indicate that circulating liquid may undergo boiling prior to supercritical fluid formation, in agreement with geochemical studies indicating that supercritical fluids can form from isobaric heating of liquid around intrusions (Heřmanská et al., 2019).

The distinctive character of the temperature field in the various Krafla subfields can be clearly linked to permeability structure. The isothermal zone temperatures in Leirbotnar require very high rock permeability ($\geq 10^{-13}$ $m^2$), which allow for the intensive vertical and horizontal convection that effectively smear out vertical temperature gradients. In addition, the low permeability aquitard lying on top of the basement intrusions reduces the input of high-enthalpy fluid from the deeper boiling reservoir to the shallow isothermal zone. Previous studies that have suggested that vertically-extensive boiling zones extending to $\geq$1 km depth, such as are found in Suðurhlíðar, require intermediate rock permea-

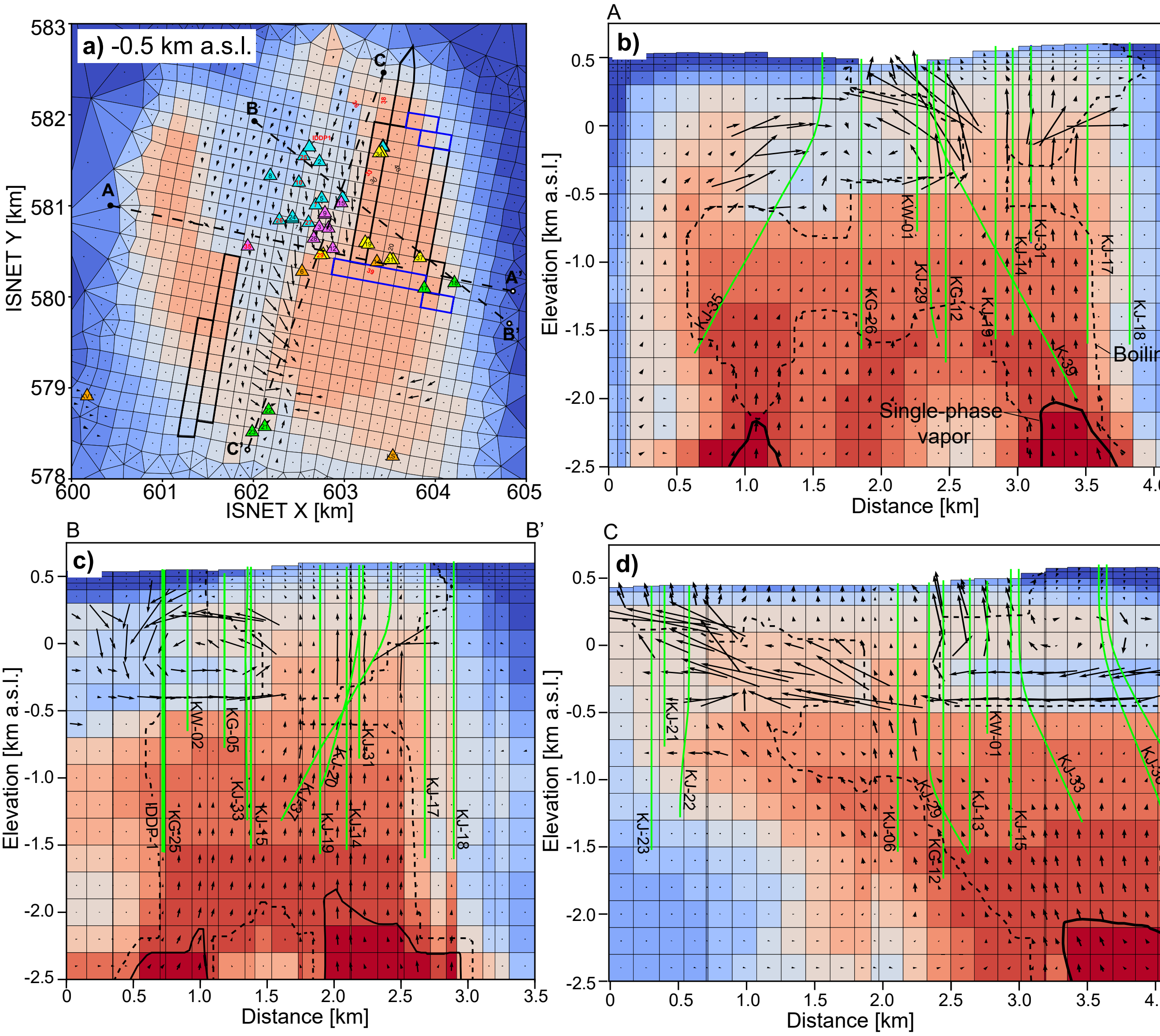


**Figure 14.** Model results from *max a posteriori* estimate. a) Depth slice at -0.5 km asl. Grid blocks modeled as fault rock types are outlined, with barrier faults outlined in black and transverse faults in blue. Well-head locations shown with triangles with same symbology as in Figure 3. b-d) Vertical cross-sections through numerical model, with traces of cross-sections shown in a). Cross-sections correspond to same cross-sections shown in Figure 4. Boiling zones are highlighted in dashed lines, zones of single-phase vapor with solid black lines. Well traces shown in green.

bility ($\sim 10^{-15}$ m$^2$) (Hayba & Ingebritsen, 1997; Scott et al., 2016). However, this study shows that such temperature contrasts can also result from spatial variations in the strength of the deep upflow, which is stronger beneath Suðurhlíðar due to higher deep mass input (Fig. 6b), as well as the lack of the low permeability aquitard in this area.

The numerical models suggest that a substantial untapped resource may be present in the Krafla area. For example, the models predict the shallow boiling zone in Suðurhlíðar extends further to the south, towards Sandabotnaskarð. Such an inference is also supported by resistivity measurements, which reveal that the areal extent of the shallow low-resistivity cap rock exceeds the present area exploited for power production, extending along the eastern rim of the caldera and to the south of Leirhnjúkur, located to the northwest of the main production area at Krafla (Árnason & Magnússon, 2001). Leirhnjúkur was a major locus of extrusive magmatism and magmatic gas discharge during the volcano-rifting event between 1975-1984 (Ármannsson et al., 1989). However, as there are no deep wells drilled into these area, it remains uncertain whether and to what extent the high-temperature system extends to this area.

## 6 Conclusions

This study has presented a new natural state model of the Krafla geothermal system. The Bayesian approach to model calibration quantifies the significant uncertainty in the model parameters. Even in an extensively drilled geothermal field such as Krafla, for which temperatures from many deep wells are available, the uncertainty in the inferred anisotropic permeability values of the different rock types is considerable, often exceeding two orders of magnitude. Moreover, fundamental restrictions on grid resolution and computational expense presently limit the ability for models to resolve small-scale permeability variations. Therefore, when harnessing modern machine learning techniques for the calibration of natural state geothermal reservoir models, a close link between the resource conceptual model and the reservoir model is essential to ensure adequate representation of the large-scale structure of the system.

The presented numerical model is one of the first to extend to the deep, supercritical roots of a system under production. However, as the role of the heat source is expressed in terms of bottom boundary conditions, fluid flow processes around the intrusive heat sources are not explicitly modeled. Moreover, geothermal systems such as Krafla undergo processes such as repeated intrusion, fracturing, and eruption over time scales of $10^2$-$10^3$ years (Thordarson & Larsen, 2007; Sparks & Cashman, 2017), and the heat of subsurface intrusions can be exhausted by hydrothermal fluid circulation on time scales of $10^3$-$10^4$ years (Scott et al., 2016), shorter than the time needed in order to reach a steady-state in the transient models (ca. $10^6$ years). Other models of cooling intrusions have shown that transient effects play a key role in governing the thermo-hydraulic structure (Scott, 2020).

In addition to better consideration of transient effects, other possibilities for future improvements could include making every block a different rock type (Bjarkason et al., 2019) and treating input mass/enthalpy as uncertain parameters (Cui et al., 2011). However, as the number of uncertain parameters increases, the connection between the reservoir model and the conceptual model becomes more tenuous, and in geothermal fields that are well-constrained by geologic and well data, incorporating such constraints in the reservoir model is valuable. In addition, the model would benefit from more data, particularly below -2 km a.s.l. Such data could become available as a result of the ongoing Krafla Magma Tested project, which aims drill several additional deep wells into the magma body in Krafla to better constrain the interface between the magmatic heat source and overlying hydrothermal system(Eichelberger et al., 2018) While the production history of this system was not used to calibrate the numerical model, this natural state model could serve a basis for the calibration of such a model. In addition, it would help evaluating whether the exploitation of the system has led to changes in the temperature distribution of the system (Guðmundsson & Arnórsson, 2002). Generally, the development of natural state model should be seen as a dynamic, iterative process, that improves as additional data becomes available and the conceptual understanding of the system deepens.

**Acknowledgments**

SWS and CC received funding from the Technical Development Fund of the Research Center of Iceland (RANNÍS—Grant Number 175193-0612 Data Fusion for Geothermal Reservoir Characterization). JPO, RN and OM received funding from the New Zealand Ministry of Business, Innovation and Employment (MBIE) through the Empowering Geothermal Energy grant. We thank Landsvirkjun for supplying the natural state temperature data, and acknowledge Vatnaskil for sharing an unpublished report outlining an earlier reservoir model of the Krafla area (Vatnaskil, 2016). Figures were made using Generic Mapping Tools v5 (Wessel et al., 2013) and PyTOUGH (Croucher, 2011). The code and data used in this study is archived at Zenodo (https://doi.org/10.5281/zenodo.5516781). The authors would like to acknowledge Knútur Árnason, Egill Júlíusson, Annette Mortensen, and Bill Cumming for helpful discussions about the structure of the Krafla system.

## References

Andrieu, C., de Freitas, N., Doucet, A., & Jordan, M. I. (2003). An introduction to MCMC for machine learning. *Machine Learning*, *50*(1), 5–43. doi: 10.1023/A:1020281327116

Aradóttir, E. S. P., Sonnenthal, E. L., Björnsson, G., & Jónsson, H. (2012). Multidimensional reactive transport modeling of CO2 mineral sequestration in basalts at the Hellisheidi geothermal field, Iceland. *International Journal of Greenhouse Gas Control*, *9*, 24–40. doi: 10.1016/j.ijggc.2012.02.006

Ármannsson, H., Benjamínsson, J., & Jeffrey, A. W. (1989). Gas changes in the Krafla geothermal system, Iceland. *Chemical Geology*, *76*, 175–196.

Ármannsson, H., Fridriksson, T., Benjamínsson, J., & Hauksson, T. (2015). History of chemical composition of geothermal fluids in Krafla, northeast Iceland, with special emphasis on the liquid phase. In *World geothermal congress 2015.*

Ármannsson, H., Fridriksson, T., Gudfinnsson, G. H., Ólafsson, M. M., Óskarsson, F., & Thorbjörnsson, D. (2014). IDDP—The chemistry of the IDDP-01 well fluids in relation to the geochemistry of the Krafla geothermal system. *Geothermics*, *49*, 66–75. doi: 10.1016/j.geothermics.2013.08.005

Ármannsson, H., Gudmundsson, Á., & Steingrímsson, B. S. (1987). Exploration and development of the Krafla geothermal area. *Jökull*, *37*, 13–29.

Árnason, K. (2020). New conceptual model for the magma-hydrothermal-tectonic system of Krafla, NE Iceland. *Geosciences*, *10*(1), 34. doi: 10.3390/geosciences10010034

Árnason, K., & Magnússon, I. T. (2001). *Resistivity measurements in Krafla (in Icelandic)* (Tech. Rep.). Reykjavik, Iceland: Orkustofnun.

Arnórsson, S. (1995). Geothermal Systems in Iceland: Structure and conceptual models-I. High-temperature areas. *Geothermics*, *24*(5), 561–602.

Aster, R. C., Borchers, B., & Thurber, C. H. (2018). *Parameter estimation and inverse problems.* Elsevier.

Axelsson, G., Egilson, T., & Gylfadóttir, S. (2014). Modelling of temperature conditions near the bottom of well IDDP-1 in Krafla, Northeast Iceland. , *49*, 49–57. doi: 10.1016/j.geothermics.2013.05.003

Bjarkason, E. K., O'Sullivan, J., Yeh, A., & O'Sullivan, M. (2019). Inverse modeling of the natural state of geothermal reservoirs using adjoint and direct methods. *Geothermics*, *78*, 85–100. doi: 10.1016/j.geothermics.2018.10.001

Björnsson, A., Sæmundsson, K., Einarsson, P., Tryggvason, E., & Grönvold, K.

(1977). Current rifting episode in north Iceland. *Nature*, *266*(5600), 318–323. doi: 10.1038/266318a0

Björnsson, G., & Bödvarsson, G. (1990). A survey of geothermal reservoir properties. *Geothermics*, *19*, 17–27.

Bödvarsson, G. S., Benson, S. M., Sigurdsson, O., Stefánsson, V., & Eliasson, E. T. (1984). The Krafla geothermal field, Iceland 1. Analysis of well test data. *Water Resources Research*, *20*(11), 1515–1530.

Croucher, A. (2011). PyTOUGH: A Python scripting library for automating TOUGH2. In *New zealand geothermal workshop.*

Croucher, A., & O'Sullivan, M. (2008). Application of the computer code TOUGH2 to the simulation of supercritical conditions in geothermal systems. *Geothermics*, *37*(6), 622–634. doi: 10.1016/j.geothermics.2008.03.005

Croucher, A., O'Sullivan, M., O'Sullivan, J., Yeh, A., & Burnell, J. (2020). Waiwera: A parallel open-source geothermal flow simulator. *Computers and Geosciences*, *141*, 104529. Retrieved from `https://doi.org/10.1016/j.cageo.2020.104529` doi: 10.1016/j.cageo.2020.104529

Cui, T., Fox, C., Nicholls, G. K., & O'Sullivan, M. (2019). Using parallel MCMC sampling to calibrate a computer model of a geothermal reservoir by using parallel MCMC sampling to calibrate a computer model of a geothermal reservoir. *International Journal for Uncertainty Quantification*, *9*(3), 295–310. doi: 10.1615/Int.J.UncertaintyQuantification.2019029282

Cui, T., Fox, C., & O'Sullivan, M. (2011). Bayesian calibration of a large-scale geothermal reservoir model by a new adaptive delayed acceptance Metropolis Hastings algorithm. *Water Resources Research*, *47*, W10521. doi: 10.1029/2010WR010352

Cui, T., Fox, C., & O'Sullivan, M. (2019). A posteriori stochastic correction of reduced models in delayed-acceptance MCMC, with application to multiphase subsurface inverse problems. *International Journal for Numerical Methods in Engineering*, *118*(10), 578–605. doi: https://doi.org/10.1002/nme.6028

Cumming, W. (2016a). 3 - Geophysics and resource conceptual models in geothermal exploration and development. In R. DiPippo (Ed.), *Geothermal power generation* (pp. 33–75). Elsevier. doi: 10.1016/B978-0-08-100337-4.00003-6

Cumming, W. (2016b). Resource capacity estimation using lognormal power density from producing fields and area from resource conceptual models: Advantages, pitfalls and remedies. In *Proceedings 41st workshop on geothermal reservoir engineering.*

Darling, W. G., & Ármannsson, H. (1989). Stable isotopic aspects of fluid flow in the Krafla, Namafjall and Theistareykir geothermal systems of northeast Iceland. *Chemical Geology*, *76*, 197–213.

Doherty, J. (2015). *Calibration and uncertainty analysis for complex environmental models.* Watermark Numerical Computing Brisbane, Australia.

Drouin, V., Sigmundsson, F., Verhagen, S., & Ófeigsson, B. G. (2017). Deformation at Krafla and Bjarnarflag geothermal areas, Northern Volcanic Zone of Iceland, 1993 – 2015. *Journal of Volcanology and Geothermal Research*, *344*, 92–105. doi: 10.1016/j.jvolgeores.2017.06.013

Eggertsson, G., Kendrick, J., Weaver, J., Wallace, P., Utley, J., Bedford, J., … Lavallée, Y. (2020). Compaction of hyaloclastite from the active geothermal system at krafla volcano, iceland. *Geofluids*, 3878503. doi: 10.1155/2020/3878503

Eggertsson, G., Lavallée, Y., Kendrick, J. E., & Markússon, S. H. (2020). Improving fluid flow in geothermal reservoirs by thermal and mechanical stimulation: The case of Krafla volcano, Iceland. *Journal of Volcanology and Geothermal Research*, *391*, 106351. doi: 10.1016/j.jvolgeores.2018.04.008

Eichelberger, J., Ingolfsson, H. P., Carrigan, C., Lavallee, Y., Tester, J. W., & Markusson, S. H. (2018). Krafla Magma Testbed: Understanding and using the magma-hydrothermal connection. In *Geothermal resources council transactions* (Vol. 42).

Einarsson, K., Pálsson, B., Gudmundsson, Á., Hólmgeirsson, S., & Ingason, K. (2010). Acid wells in the Krafla geothermal field. In *World geothermal congress 2010* (pp. 25–29).

Einarsson, P. (1978). S-wave shadows in the Krafla caldera in NE-Iceland, evidence for a magma chamber in the crust. *Bulletin Volcanologique*, *41*(1958), 187–195.

Einarsson, P. (1991). Earthquakes and present-day tectonism in Iceland. *Tectonophysics*, *189*, 261–279.

Einarsson, P. (2008). Plate boundaries, rifts and transforms in Iceland. *Jökull*, *58*, 35–58.

Elders, W. A., Friðleifsson, G. O., Zierenberg, R. A., Pope, E. C., Mortensen, A. K., Guðmundsson, A., ... Schiffman, P. (2011). Origin of a rhyolite that intruded a geothermal well while drilling at the Krafla volcano, Iceland. *Geology*, *39*(3), 231–234. doi: 10.1130/G31393.1

Finsterle, S. (2007). *iTOUGH2 User's Guide* (Tech. Rep.). Berkeley, California: Lawrence Berkeley National Laboratory.

Flóvenz, Ó. G., & Saemundsson, K. (1993). Heat flow and geothermal processes in Iceland. *Tectonophysics*, *225*(1-2), 123–138. doi: 10.1016/0040-1951(93)90253-G

Foreman-Mackey, D., Hogg, D. W., Lang, D., & Goodman, J. (2013). emcee: The MCMC hammer. *Publications of the Astronomical Society of the Pacific*, *125*(925), 306–312. doi: 10.1086/670067

Gelman, A., Carlin, J. B., Stern, H. S., Dunson, D. B., Vehtari, A., & Rubin, D. B. (2013). *Bayesian data analysis.* CRC press.

Gelman, A., & Hill, J. (2006). *Data analysis using regression and multilevel/hierarchical models.* Cambridge University Press.

Gelman, A., Roberts, G., & Gilks, W. (1996). Efficient metropolis jumping rules. *Bayesian statistics*.

Goodman, J., & Weare, J. (2010). Ensemble samplers with affine invariance. *Communications in applied mathematics and computational science*, *5*(1), 65–80.

Grant, M. A., Bixley, P. F., Donaldson, I. G., & Bixley, P. F. (2011). *Geothermal Reservoir Engineering* (Second Edition ed.). Academic Press. doi: https://doi.org/10.1016/B978-0-12-383880-3.10002-2

Gunnarsson, G., Arnaldsson, A., & Oddsdóttir, A. L. (2010). Model simulations of the Hengill area, southwestern Iceland. *Transport in Porous Media*, *90*, 3–22. doi: 10.1007/s11242-010-9629-1

Guðmundsson, B. T., & Arnórsson, S. (2002). Geochemical monitoring of the Krafla and Namafjall geothermal areas, N-Iceland. *Geothermics*, *31*(2), 195–243.

Gylfadóttir, S. S. (2013). *Modeling the Námafjall Geothermal System* (Tech. Rep.). Reykjavik, Iceland: Iceland GeoSurvey.

Hayba, D. O., & Ingebritsen, S. E. (1997). Multiphase groundwater flow near cooling plutons. *Journal of Geophysical Research*, *102*(B6), 12235–12252. doi: 10.1029/97JB00552

Heap, M. J., Gravley, D. M., Kennedy, B. M., Gilg, H. A., Bertolett, E., & Barker, S. L. L. (2020). Quantifying the role of hydrothermal alteration in creating geothermal and epithermal mineral resources: The Ohakuri ignimbrite (Taupō Volcanic Zone, New Zealand). *Journal of Volcanology and Geothermal Research*, *390*, 106703. doi: https://doi.org/10.1016/j.jvolgeores.2019.106703

Heřmanská, M., Stefánsson, A., & Scott, S. (2019). Supercritical fluids around magmatic intrusions: IDDP-1 at Krafla, Iceland. *Geothermics*, *78*, 101–110. doi: 10.1016/j.geothermics.2018.11.002

Hjartardóttir, Á. R., Einarsson, P., Bramham, E., & Wright, T. J. (2012). The Krafla fissure swarm, Iceland, and its formation by rifting events. *Bulletin of*

*Volcanology*, *74*(9), 2139–2153. doi: 10.1007/s00445-012-0659-0

Hjartardóttir, Á. R., Einarsson, P., Magnúsdóttir, S., Björnsdóttir, T., & Brandsdóttir, B. (2016). Fracture systems of the Northern Volcanic Rift Zone, Iceland: an onshore part of the Mid-Atlantic plate boundary. *Geological Society, London, Special Publications*, *420*(1), 297–314.

Ingason, K., Kristjánsson, V., & Einarsson, K. (2014). Design and development of the discharge system of IDDP-1. *Geothermics*, *49*, 58–65. doi: 10.1016/j.geothermics.2013.05.002

Ingebritsen, S. E., & Manning, C. E. (2010). Permeability of the continental crust: dynamic variations inferred from seismicity and metamorphism. *Geofluids*, *10*, 193–205. doi: 10.1111/j.1468-8123.2010.00278.x

Jakobsson, S. P., & Guðmundsson, M. T. (2008). Subglacial and intraglacial volcanic formations in Iceland. *Jökull*, *58*, 179–196.

Jolie, E., Scott, S., Faulds, J. E., Chambefort, I., Axelsson, G., Gutiérrez-Negrín, L. C., ... Ayling, B. (2021). Geological controls on geothermal resources for power generation. *Nature Reviews Earth and Environment*, *2*, 324–339. doi: 10.1038/s43017-021-00154-y

Jónasson, K. (1994). Rhyolite volcanism in the Krafla central volcano, north-east Iceland. *Bulletin of Volcanology*, *56*(6), 516–528. doi: 10.1007/BF00302832

Kaipio, J., & Somersalo, E. (2006). *Statistical and computational inverse problems* (Vol. 160). Springer Science & Business Media.

Kaipio, J., & Somersalo, E. (2007). Statistical inverse problems: Discretization, model reduction and inverse crimes. *Journal of Computational and Applied Mathematics*, *198*, 493–504. doi: 10.1016/j.cam.2005.09.027

Khodayar, M., Björnsson, S., Kristinsson, S. G., Karlsdóttir, R., Ólafsson, M., & Víkingsson, S. (2018). Tectonic control of the Theistareykir geothermal field by rift and transform zones in North Iceland: A multidisciplinary approach. *Open Journal of Geology*, *8*(6), 543–584. doi: 10.4236/ojg.2018.86033

Kim, D., Brown, L. D., Árnason, K., Águstsson, K., & Blanck, H. (2017). Magma reflection imaging in Krafla, Iceland using microearthquake sources. *Journal of Geophysical Research*, *122*, 1–15. doi: 10.1002/2016JB013809

Kim, D., Brown, L. D., Árnason, K., Gudmundsson, Ó., Ágústsson, K., & Flóvenz, Ó. G. (2018). Magma "bright spots" mapped beneath Krafla, Iceland, using RVSP imaging of reflected waves from microearthquakes. *Journal of Volcanology and Geothermal Research*. doi: 10.1016/j.jvolgeores.2018.04.022

Kondo, K., Itoi, R., Tanaka, T., & Iwasaki, T. (2017). Numerical simulation of the Sumikawa geothermal reservoir, Japan, using iTOUGH2. In *Proceedings 42nd geothermal workshop on geothermal reservoir engineering.*

Kristmannsdóttir, H. (1979). Alteration of basaltic rocks by hydrothermal activity at 100-300 C. *Developments in Sedimentology*, *27*, 359–367.

Lamur, A., Kendrick, J. E., Eggertsson, G. H., Wall, R. J., Ashworth, J. D., & Lavallée, Y. (2017). The permeability of fractured rocks in pressurised volcanic and geothermal systems. *Scientific Reports*, *7*, 6173. doi: 10.1038/s41598-017-05460-4

Larsen, G., Grönvold, K., & Thorarinsson, S. (1979). Volcanic eruption through a geothermal borehole at Námafjall, Iceland. *Nature*, *278*(5706), 707–710. doi: 10.1038/278707a0

Lee, B., Unsworth, M., Árnason, K., & Cordell, D. (2020). Imaging the magmatic system beneath the Krafla geothermal field, Iceland: A new 3-D electrical resistivity model from inversion of magnetotelluric data. *Geophysical Journal International*, *220*, 541–567. doi: 10.1093/gji/ggz427

Liotta, D., Brogi, A., Árnadóttir, S., Ágústsson, K., & Thorsteinsdóttir, U. (2021). Field evidence of the interplay between rift and transform structures in the Krafla geothermal area, N-Iceland. *Geothermics*, *91*, 102039. doi: 10.1016/j.geothermics.2020.102039

Maclaren, O. J., Nicholson, R., Bjarkason, E. K., O'Sullivan, J., & O'Sullivan, M. (2020). Incorporating posterior-informed approximation errors into a hierarchical framework to facilitate out-of-the-box MCMC sampling for geothermal inverse problems and uncertainty quantification. *Water Resources Research*, *56*, e2018WR024240. doi: 10.1029/2018WR024240

Magnusdóttir, L., & Finsterle, S. (2015). An iTOUGH2 equation-of-state module for modeling supercritical conditions in geothermal reservoirs. *Geothermics*, *57*, 8–17. doi: 10.1016/j.geothermics.2015.05.003

Mannington, W., O'Sullivan, M., & Bullivant, D. (2004). Computer modelling of the Wairakei-Tauhara geothermal system, New Zealand. *Geothermics*, *33*(4), 401–419. doi: 10.1016/j.geothermics.2003.09.009

Metropolis, N., Rosenbluth, A. W., Rosenbluth, M. N., Teller, A. H., & Teller, E. (1953). Equation of state calculations by fast computing machines. *The journal of chemical physics*, *21*(6), 1087–1092.

Milicich, S. D., Pearson-Grant, S. C., Alcaraz, S., White, P. A., & Tschritter, C. (2018). 3D Geological modelling of the Taupo Volcanic Zone as a foundation for a geothermal reservoir model. *New Zealand Journal of Geology and Geophysics*, *1*, 79-95. doi: 10.1080/00288306.2017.1407346

Moon, H., Clearwater, J., Franz, P., Wallis, I., & Azwar, L. (2014). Sensitivity analysis, parameter estimation and uncertainty propagation in a numerical model of the Ngatamariki geothermal field, New Zealand. In *Proceedings of 39th stanford geothermal workshop* (pp. 1–10).

Mortensen, A. K., Egilson, T., Gautason, B., Árnadöttir, S., & Guðmundsson, A. (2014). Stratigraphy, alteration mineralogy, permeability and temperature conditions of well IDDP-1, Krafla, NE-Iceland. *Geothermics*, *49*, 31–41. doi: 10.1016/j.geothermics.2013.09.013

Mortensen, A. K., Grönvold, K., Gudmundsson, Á., Steingrímsson, B., & Egilson, Þ. (2010). Quenched silicic glass from well KJ-39 in Krafla, North-Eastern Iceland. In *World geothermal congress 2010.*

Mortensen, A. K., Guðmundsson, Á., Steingrímsson, B., Sigmundsson, F., Axelsson, G., Ármannsson, H., … Hauksson, T. (2009). *Jarðhitakerfið í Kröflu. Samantekt rannsókna á jarðhitakerfinu og endurskoðað hugmyndalíkan* (Tech. Rep.). Reykjavik, Iceland: Landsvirkjun.

Mortensen, A. K., Guðmundsson, Á., Steingrímsson, B., Sigmundsson, F., Axelsson, G., Ármannsson, H., … Hauksson, T. (2015). *The Krafla Geothermal System: Research Summary and Conceptual model revision* (Tech. Rep.). Reykjavik, Iceland: Landsvirkjun.

Mosegaard, K., & Sambridge, M. (2002). Monte Carlo analysis of inverse problems. *Inverse Problems*, *18*(3), 29–54. doi: 10.1088/0266-5611/18/3/201

Narasimhan, T. N., & Witherspoon, P. A. (1976). An integrated finite difference method for analyzing fluid flow in porous media. *Water Resources Research*, *12*(1), 57–64. doi: https://doi.org/10.1029/WR012i001p00057

Newson, J., Mannington, W., Sepulveda, F., Lane, R., Clearwater, E., & O'Sullivan, M. (2012). Application of 3D modelling and visualization software To reservoir simulation: Leapfrog Geothermal and Tough2. In *Thirty-seventh workshop on geothermal reservoir engineering.*

Oskarsson, N. (1984). Monitoring of fumarole discharge during the 1975-1982 rifting in Krafla volcanic center, North Iceland. *Journal of Volcanology and Geothermal Research*, *22*, 97–121.

O'Sullivan, J., Croucher, A., Popineau, J., Yeh, A., & O'Sullivan, M. (2019). Working with multi-million block geothermal reservoir models. In *Proceedings of the 44th workshop on geothermal reservoir engineering.*

O'Sullivan, J., Kipyego, E., Croucher, A., Ofwona, C., & O'Sullivan, M. (2015). A supercritical model of the Menengai geothermal system. In *World geothermal congress.*

O'Sullivan, J., Newson, J., Alcaraz, S., Barton, S., Baraza, R., Croucher, A., ... O'Sullivan, M. (2020). A robust supercritical geothermal simulator. In *New zealand geothermal workshop.*

O'Sullivan, J., O'Sullivan, M., & Croucher, A. (2016). Improvements to the AUTOUGH2 supercritical simulator with extension to the air-water equation-of-state. In *Geothermal resources council transactions* (pp. 921–930).

O'Sullivan, M., & O'Sullivan, J. (2016). Reservoir modeling and simulation for geothermal resource characterization and evaluation. In R. DiPippo (Ed.), *Geothermal power generation* (pp. 165–199). Elsevier. doi: 10.1016/B978-0-08-100337-4.00007-3

O'Sullivan, M., Pruess, K., & Lippmann, M. J. (2001). State of the art of geothermal reservoir simulation. *Geothermics*, *30*(4), 395–429. doi: 10.1016/S0375-6505(01)00005-0

Plasencia, M., Pedersen, A., Arnaldsson, A., Berthet, J. C., & Jónsson, H. (2014). Geothermal model calibration using a global minimization algorithm based on finding saddle points and minima of the objective function. *Computers and Geosciences*, *65*, 110–117. doi: 10.1016/j.cageo.2013.09.007

Pope, E. C., Bird, D. K., Arnórsson, S., & Giroud, N. (2015). Hydrogeology of the Krafla geothermal system, northeast Iceland. *Geofluids*, *16*, 175–197. doi: 10.1111/gfl.12142

Popineau, J., O'Sullivan, J., O'Sullivan, M., & Archer, R. (2018). An Integrated Leapfrog/TOUGH2 Workflow for a Geothermal Production Modelling. *Proceedings 7th African Rift Geothermal Conference*, 1–13.

Prasetyo, F., O'Sullivan, J., & O'Sullivan, M. (2016). Inverse modelling of Lahendong geothermal field. In *Proceedings 38th new zealand geothermal workshop.*

Pruess, K. (1991). *TOUGH2- A general-purpose numerical simulation for multiphase fluid and heat flow* (Tech. Rep.). Lawrence Berkeley Laboratory.

Pruess, K., Oldenburg, C., & Moridis, G. (2012). *TOUGH2 User's Guide, Version 2* (Tech. Rep. No. November 1999). Berkeley, California: Earth Sciences Division, Lawrence Berkeley National Laboratory, University of California.

Ratouis, T. M., O'Sullivan, M., & O'Sullivan, J. (2016). A Numerical model of Rotorua Geothermal Field. *Geothermics*, *60*, 105–125. doi: 10.1016/j.geothermics.2015.12.004

Reid, L. B., & Wellmann, J. F. (2012). Basin-scale geothermal model calibration using iTOUGH2. In *Tough symposium 2012.*

Rooyakkers, S. M., Stix, J., Berlo, K., Petrelli, M., & Sigmundsson, F. (2021). Eruption risks from covert silicic magma bodies. *Geology*, *49*. doi: 10.1130/G48697.1

Sæmundsson, K. (1991). Geology of the Krafla system. *The Natural History of Lake Myvatn*, 24–95.

Sæmundsson, K. (2008). *Krafla. Geological Map, 1:25000* (Tech. Rep.). Reykjavik, Iceland: Landsvirkjun and Iceland GeoSurvey.

Schuler, J., Pugh, D. J., Hauksson, E., White, R. S., Stock, J. M., & Brandsdóttir, B. (2016). Focal mechanisms and size distribution of earthquakes beneath the Krafla central volcano, NE Iceland. *Journal of Geophysical Research: Solid Earth*, *121*(7), 5152–5168. doi: 10.1002/2016JB013213

Scott, S. (2020). Decompression boiling and natural steam cap formation in high-enthalpy geothermal systems. *Journal of Volcanology and Geothermal Research*, *395*, 106765. doi: 10.1016/j.jvolgeores.2019.106765

Scott, S., Covell, C., Júlíusson, E., Valfells, Á., Newson, J., Hrafnkelsson, B., & Gudjónsdóttir, M. (2019). A probabilistic geologic model of the Krafla geothermal system constrained by gravimetric data. *Geothermal Energy*, *7*(29). doi: 10.1186/s40517-019-0143-6

Scott, S., Driesner, T., & Weis, P. (2015). Geologic controls on supercritical geothermal resources above magmatic intrusions. *Nature Communications*, *6*, 7837.

doi: 10.1038/ncomms8837

Scott, S., Driesner, T., & Weis, P. (2016). The thermal structure and temporal evolution of high-enthalpy geothermal systems. *Geothermics*, *62*, 33–47. doi: 10.1016/j.geothermics.2016.02.004

Sparks, R. S. J., & Cashman, K. V. (2017). Dynamic magma systems: Implications for forecasting volcanic activity. *Elements*, *13*(1), 35–40. doi: 10.2113/gselements.13.1.35

Stefánsson, V. (1981). The Krafla geothermal field, northeast Iceland. In L. Rybach & L. J. P. Muffler (Eds.), *Geothermal systems: Principles and case studies* (pp. 273–293). New York: Wiley-Interscience.

Stimac, J., Goff, F., & Goff, C. J. (2015). Intrusion-related geothermal systems. In H. Sigurðsson, B. Houghton, H. Rymer, J. Stix, & S. McNutt (Eds.), *The encyclopedia of volcanoes* (Second ed., pp. 799–822). Elsevier. doi: 10.1016/B978-0-12-385938-9.00046-8

Sveinbjörnsdóttir, Á. (1992). Composition of geothermal minerals from saline and dilute fluids — Krafla and Reykjanes, Iceland. *Lithos*, *27*, 301–315.

Sveinbjörnsdóttir, A. E., Coleman, M. L., & Yardley, B. W. D. (1986). Origin and history of hydrothermal fluids of the Reykjanes and Krafla geothermal fields, Iceland: A stable isotope study. *Contributions to Mineralogy and Petrology*, *94*, 99–109.

Tarantola, A. (2005). *Inverse problem theory and methods for model parameter estimation.* Society for Industrial and Applied Mathematics. doi: 10.1137/1.9780898717921

Thien, B. M. J., Kosakowski, G., & Kulik, D. (2015). Differential alteration of basaltic lava flows and hyaloclastites in Icelandic hydrothermal systems. *Geothermal Energy*, *3*(1), 11. doi: 10.1186/s40517-015-0031-7

Thordarson, T., & Larsen, G. (2007). Volcanism in Iceland in historical time: Volcano types, eruption styles and eruptive history. *Journal of Geodynamics*, *43*, 118–152. doi: 10.1016/j.jog.2006.09.005

Vatnaskil. (2016). *Simulation of the Krafla geothermal system* (Tech. Rep. No. 16).

Weaver, J., Eggertsson, G., Utley, J. E., Wallace, P. A., Lamur, A., Kendrick, J. E., ... Lavallée, Y. (2020). Thermal liability of hyaloclastite in the Krafla geothermal reservoir, Iceland: The impact of phyllosilicates on permeability and rock strength. *Geofluids*, 9057193. doi: 10.1155/2020/9057193

Weisenberger, T., Axelsson, G., Arnaldsson, A., Blischke, A., Óskarsson, F., Ármannsson, H., ... Guðmundsdóttir, V. (2015). *Revision of the Conceptual Model of the Krafla Geothermal System* (Tech. Rep.). Reykjavik, Iceland: Landsvirkjun.

Weisenberger, T., & Selbekk, R. S. (2009). Multi-stage zeolite facies mineralization in the Hvalfjördur area, Iceland. *International Journal of Earth Sciences*, *98*(5), 985–999. doi: 10.1007/s00531-007-0296-6

Wessel, P., Smith, W. H., Scharroo, R., Luis, J., & Wobbe, F. (2013). Generic mapping tools: Improved version released. *Eos*, *94*(45), 409–410. doi: 10.1002/2013EO450001

Yeh, A., Croucher, A., & O'Sullivan, M. (2012). Recent developments in the AUTOUGH2 simulator. In *Proceedings tough symposium 2012.*